UNIVERSIDAD CARLOS III DE MADRID
ESCUELA POLITÉCNICA SUPERIOR

uc3m

Design of flapping wing kinematics
for trimmed flight

Bachelor Thesis

Author
Daniel Morón Montesdeoca

Supervisor
Oscar Flores Arias

Leganés, June 2017

Department of Aerospace Engineering
ESCUELA POLITÉCNICA SUPERIOR

Design of flapping wing kinematics
for trimmed flight

Bachelor in Aerospace Engineering

Author
Daniel Morón Montesdeoca

Supervisor
Oscar Flores Arias

Leganés, June 2017

List of Figures

List of Tables

Acknowledgements

Contents

Chapter 1

Introduction

Unmanned aerial vehicles, commonly known as drones, represent a fast growing industry in today's aeronautical engineering [20, 12]. Drones are mainly related with surveillance, military, leisure and security activities, but future developments may probably lead them to play major roles in other fields, such as search and rescue activities, mining or agriculture [13].

Drones come in several types, one of them are the Micro-Air Vehicles (MAVs), tiny robots which can use rotary, fixed or flapping wings. It is believed that the today's typical fixed wing or rotary wing MAVs loose their advantage in terms of efficiency and manoeuvring to the flapping wing models [26]. Fast manoeuvring flying insects are a living proof to this statement.

As evidence suggests, flying insects have been around for 350 millions of years [19]. During that time they have evolved to reach outstanding manoeuvring, stability and flight control capabilities. We, humans, have always been fascinated by natural fliers, and struggled to understand their flying mechanisms.

These animals make use of flying mechanisms and control systems that are not yet well understood. They are an open and wide field of study on today's aeronautical engineering.

1.1   Current challenges

The wings of flying insects are the surfaces responsible for generating the aerodynamic forces that keep the animal aloft (lift), and also counteract the associated drag to their movement, (thrust). The conventional inviscid steady aerodynamic theory used for airplanes fails to describe how these natural fliers are able to generate these needed forces. That is because flying insects take advantage of some unsteady and viscous mechanisms that are neglected in the classical fixed wing theory [3, 2, 30]. These mechanisms have been determined to account for up to a 30% of the total force generated during a stroke, but they are rather difficult to model in a preliminary design.

Insects wings are made of flexible and elastic membranes that can freely adapt their shape to each flow condition. Insects do not only choose the best combination of wing kinematics to produce the required unsteady mechanisms to stay aloft, but they also use the deformation of their wings,

to enhance the aerodynamic forces [30]. In fact it is currently being studied whether the flexibility of the wings may play a major role on the stability of flying insects [7].

Furthermore insects make use of sensory control systems, that allow them to detect changes in flow patterns and adjust their stroke in order to stabilize themselves or quickly avoid an object [29].

1.2 State of the art

The advances in photography and particle tracking have allowed investigators to better determine the wing kinematics of flying insects, and their resultant flow characteristics. Recently, such a study has been performed on mosquitoes to explain how, with their relatively short wings and long body, they are able to stay aloft, [8]. The observed kinematics can then be used to define quasi-steady models that approximate the aerodynamic forces [3]. This is the usual strategy to determine models that allow to perform stability or parameters analyses, but there are other approaches [32].

Despite the complexity it entails, actual flapping wing MAVs have been recently designed. *Delft University* includes a program called the *DelFLY Project*, that has built several flapping wing MAVs with control tails, among which we can find the latest *DelFLY Explorer*, capable of peforming autonomous flight [10]. *Harvard University* has developed a tailless MAV called *Robobee* that is able to fly while wired and to even cling to surfaces [34]. More recently a team of *Konkuk University*, in Seoul has developed a tailless model capable of autonomously climb, hover and loiter with the use of attitude controllers [27].

In the first stages of any MAV design, it could be interesting to define what are the flight conditions the design is expected to fly, and calculate the trim variables that are needed in order to reach them. These analyses would give some gross numbers, for instance in terms of required power or forces, that could point the directions the rest of the design shall follow. The method proposed by [5] computes the aerodynamic forces for different flapping cases using a CFD method, and then looks for the trim variables that allow to obtain steady flight conditions with the use of a quasi-steady model.

1.3 Objectives

The main objective of this project is to develop a numerical tool using MATLAB@ that calculates a set of initial conditions and wing kinematic parameters that result in a trimmed flight for a given flapping wing MAV model. The project adapts the unsteady panel method developed by [4] to obtain the aerodynamic forces of the wings, and the dynamic model developed by [25], to integrate these forces and obtain the movement of the model with time.

The tool is meant to be used at the first stages of the design of a given MAV, in order to check the general effects of a selected geometry and the impact that some parameters may have on the performance. A second requirement is to obtain a tool that is able to perform such a high number of analyses without a high computation time/cost, but being as rigorous as possible.

1.4 Socio-economic impact

As we have stated above the tool is aimed to be used in the preliminary design of a given flapping MAV. Although the technology of these small air vehicles is still pretty young, they are expected to play major roles in the future drone industry.

Unmanned flying vehicles, as we briefly mentioned earlier, are being used for a diverse collection of activities, like surveillance. One example is the use of these drones to monitor the changes in biodiversity of given locations [22]. They are also growing in importance in the audiovisual industry, where they allow to obtain valuable shots of, for instance sport events, or short videos uploaded in the Internet.

The quick response and performance of future insect-like robots will surely fit right in these activities. The potential of flapping MAVs, however, should not only be reduced to their small size and remarkable manoeuvrability. Current lines of investigation are trying to code a set of drones so they can perform manoeuvres simultaneously. In the future these *flocks* of MAVs could carry bigger objects or, for instance, detect chemical hazards on huge zones [13].

The development of these technologies could also have some drawbacks. It is well known the use of drones to deliver packages for businesses like *Amazon* and *DHL*, but it has also been suggested to use these unmanned vehicles to deliver postal-office too. The increasing number of drones may lead to an uncontrolled traffic that could pose a threat to public safety.

1.5 Regulations and legal framework

Regarding the regulations that could affect future flapping MAVs, we should review the current legal framework of unmanned aircraft. It must be noted that the industry is a fast moving one that complicates the work of the airworthiness authorities, as new advances and technologies are developed faster than they can regulate them. Back in 2011, the International Civil Aviation Organization (ICAO), considered a first attempt to develop a global legal framework for drones, and efforts are still being made.

Spain's government published a first law regarding unmanned flying vehicles back in 2014. The law, that has been several times modified, formulates some rules that must be followed when drones are operated in Spanish airspace [1]. It differentiates between commercial and leisure uses, and distinguishes between types of drones, giving boundaries and limits of operations for all cases. It also requires pilots, that are going to use drones for economic issues, to obtain a license.

Other countries of the European Union have also developed some rules and regulations, resulting in a non-homogeneous legal framework in the whole community. In order to amend that, the European Aviation Safety Agency (EASA) is developing a proposal that concerns all member states, and that aims to offer a framework that not only ensures the safe operation of drones, but also allows the industry to remain agile and continue to grow. The proposal is meant to be submitted to the European Union Commission by the end of 2017 [12].

Chapter 2

Definition of the vehicle

Before designing the desired numerical tool, we need to define a flapping wing MAV model. In this chapter the kinematics, geometry and mass characteristics of the chosen model are defined. The MAV will be modelled as a rigid body, which has attached two massless wings. It will be inspired on a *Drosophila melanogaster*, also known as the fruit fly.

2.1 Body

The mass characteristics of our MAV have been obtained from the experimental data included in [9]. The total mass of the vehicle and the values of the elements of the tensor of inertia are presented below:

- Mass $m = 9.6 \cdot 10^{-7} kg$

- Inertia Tensor

    - $I_{xx} = 3.06 \cdot 10^{-13} Nms^2$

    - $I_{yy} = 5.06 \cdot 10^{-13} Nms^2$

    - $I_{zz} = 3.06 \cdot 10^{-13} Nms^2$

    - $I_{xz} = -1.91 \cdot 10^{-13} Nms^2$

    - $I_{xy} = I_{zy} = 0$

Regarding the aerodynamics forces of the body, only the parasitic body drag has been modelled. When calculating the drag, the body is assumed to be shaped as a cylinder with rounded extremes (similar to an ellipsoid). The drag acts directly on the center of gravity of the vehicle, which is located at the center of symmetry of the cylinder. The dimensions are:

$$L_{body} = 3.4mm \text{ and } D_{body} = 1.04mm \tag{2.1}$$

The length L_{body} and diameter D_{body} of the body have been determined graphically, from the value of other parameters, like the chord or span of the wings.

2.2 Wings

The wings are the moving surfaces relative to the body that are in charge of producing the aerodynamic forces. This project defines two symmetric wings greatly inspired by the shape of the wings of a *Drosophila melanogaster*. They are defined as finite surfaces, without mass, inertia, thickness or camber.

Regarding the design of the wing, several parameters have to be defined:

- Wing Span, is the length of the wing measured from one tip to another. In this project the wing span will refer to the distance measured from the root to the tip of each wing, b_w.

- Surface S, total area of each wing.

- Aspect Ratio AR, which relates the wing span with its surface. This parameter is a key design value that is strongly related with the aerodynamic and structural requirements of a wing. In our case the aspect ratio is defined as:

$$AR = \frac{b_w^2}{S} \tag{2.2}$$

- Chord of the wing, or the distance between the leading edge and trailing edge at any span-wise position. The leading edge defines the part of the wing that firstly comes in contact with the incoming flow, while the trailing edge comes in contact with the flow the last. An important parameter from the point of view of aerodynamics is the mean aerodynamic chord MAC, which is defined as the chord-weighted average of the wing. In this project it is assumed that the MAC is equal to the mean geometric chord and calculated as:

$$MAC = \frac{S}{b_w} = \frac{b_w}{AR} \tag{2.3}$$

Let us denote the MAC as c.
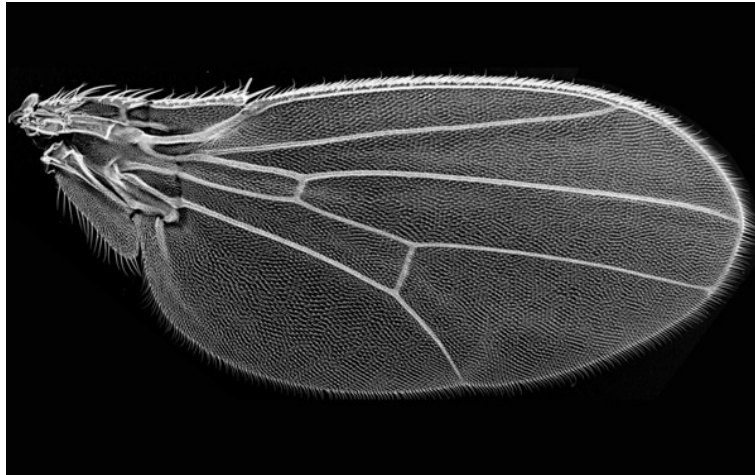
Figure 2.1: Typical fruit fly wing.

The shape of our wing has been defined as follows:
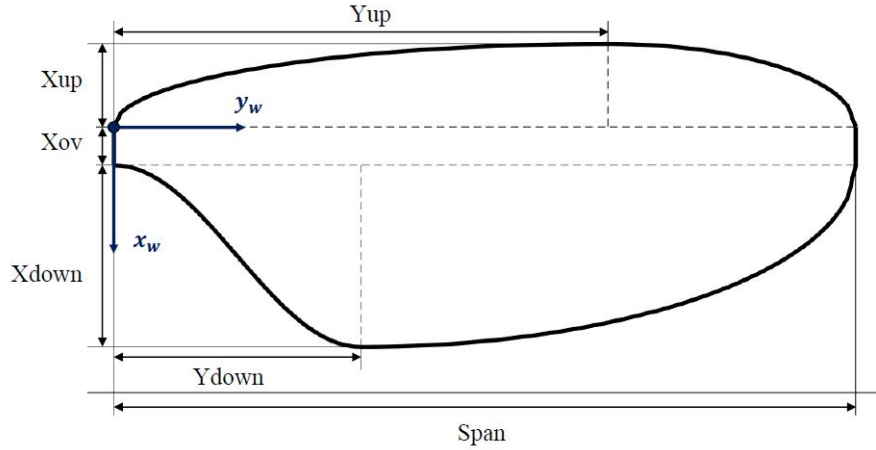
Figure 2.2: Our modelled wing. The attached reference frame points from the root to the tip (y_w direction) and from the leading edge to the trailing edge (x_w direction).

- The leading edge is defined with the use of two quarters of two different ellipses.

  1. For $y_w \in [0, Y_{up}]$ the shape is that of an ellipse, named ellipse 1, whose axis are: $2 \cdot X_{up}$ and $2 \cdot Y_{up}$.

  2. For $y_w \in [Y_{up}, b_w]$ the shape is that of an ellipse, named ellipse 2, whose axis are: $2 \cdot X_{up}$ and $2 \cdot (b_w - Y_{up})$.

- The value X_{over} stands for the overshoot that separates the trailing and leading edges at the root and tip of the wing.

- The trailing edge is defined with the use of a quarter of ellipse and the arc length of a sinusoidal expression.

  1. For $y_w \in [Y_{down}, b_w]$ the shape is that of an ellipse, named ellipse 3, whose axis are: $2 \cdot X_{down}$ and $2 \cdot (b_w - Y_{down})$.

  2. For $y_w \in [0, Y_{down}]$ a new function different to an ellipse was defined so the final design was as similar as possible to the real case. Moreover this function had to have a smooth joint to ellipse number 3, with the same slope at that position. A function that compiled with both requirements was determined to be:

$$X_{w_{TE}} = X_{down} \cdot \sin^2 \left(\frac{\pi \cdot y_w}{2 \cdot Y_{down}} \right) \tag{2.4}$$

The key parameters that define the shape of our wing were determined as follows:

1. Firstly the wing span and Aspect Ratio were selected. From those two values the c and S can be calculated (Equations: (2.2) and (2.3)).

2. Some parameters are defined after a trial and error analysis, looking for the more approximate layout possible. One possible combination is the one selected for this project

   - $X_{ov} = 16.8\%c$ and $X_{down} = 79.33\%c$.

- $Y_{up} = 66.66\% b_w$ and $Y_{down} = 33.33\% b_w$.

3. Finally X_{up} is obtained so the total sum of the areas of the sections equals the objective value of the surface of the wing. Recall that the area of an ellipse is given by: $A = \pi \cdot a \cdot b$ being a and b the major semi axes of the ellipse. It can also be checked that the integral of the sinusoidal function, inside the defined boundaries, is equal to $\frac{X_{down} \cdot Y_{down}}{2}$.

$$S = X_{ov} \cdot b_w + \frac{X_{down} \cdot Y_{down}}{2} + \frac{\pi}{4} \cdot X_{down} \cdot (b_w - Y_{down}) + \frac{\pi}{4} \cdot X_{up} \cdot (Y_{up}) + \frac{\pi}{4} \cdot X_{up} \cdot (b_w - Y_{up}) \quad (2.5)$$

$$X_{up} = \frac{4}{\pi \cdot b_w} \cdot \left(\frac{b_w^2}{AR} - X_{ov} \cdot b_w - \frac{X_{down} \cdot Y_{down}}{2} - \frac{\pi}{4} \cdot X_{down} \cdot (b_w - Y_{down}) \right) \quad (2.6)$$

The selected aspect ratio and wing span are those used by [5] $AR = 2.8$ and $b_w = 3mm$. Although the reference frame of the wing is presented attached to a point in its root, figure (2.2), during this project the origin of the reference frame will be located inside the body, and the origin of the wing will be at a distance $y_w = y_1$ outboard, from that point.

We have already mentioned the mass characteristics and geometry of our wings and body, but we have not defined where the wings will be attached with respect to the center of mass G. Let us firstly define the different reference frames that are going to be used in this project.

2.3   Reference frames

- Let us define an arbitrary Inertial Reference Frame (IRF) cantered in I with orthogonal axes X, Y and Z, with respect to which the movement of the center of mass of the vehicle, G, will be defined. The position vector of G at any instant of time will be given as: $\vec{x}_G = [x_G, y_G, z_G]$.

- Attached to the body a reference frame is defined with its origin at G. The axes of this second reference frame are: x_{cg}, y_{cg} and z_{cg}, where axis x_{cg} is parallel to the revolution axis of the idealised cylinder. Let us name this reference frame as the *body axis reference frame*.

- Two reference frames are defined, attached to each wing and with axes $x_{w_{R/L}}, y_{w_{R/L}}$ and $z_{w_{R/L}}$. R/L stands for right or left wing. Axis y_w of the right wing runs along the span, from the root to the tip, while the one of the left wing goes from the tip to the root. Axis x_w of both wings point from the leading edge to the trailing edge, and z_w is normal to the surface and perpendicular to the other two. The line defined for $x_w = z_w = 0$ for each wing has been selected so it is mainly located closer to the $25\% c$ of each spanwise section. Both reference frames are centred in a point O, that is inside the body. The position vector of point O with respect to G in body axis is defined as:

$$\vec{x}_{O/G} = \begin{bmatrix} x_{O/G} \\ y_{O/G} \\ z_{O/G} \end{bmatrix} \quad (2.7)$$

In this project $z_{O/G} = y_{O/G} = 0$ and $x_{O/G} = 0.25 \cdot c - d_{O/G}$ where $d_{O/G}$ has been obtained from [5] and it is equal to $0.3mm$. Please bare in mind that the origin of each wing will be

placed just outside the body, at the same distance with respect to *O*. For instance for the right wing the coordinate that gives the first point at the root of the wing in wing axis is $[0, y_1, 0]$. The parameter y_1 is positive for the right wing and negative for the left, and its magnitude is a half of the maximum width of the thorax, (D_{body}).

- At the point *O* another reference frame may be defined, so its axes are parallel to the ones of the body reference frame. This reference frame could be helpful in case both wings are not centred at the same position. Despite it is not used in this project it is also mentioned.
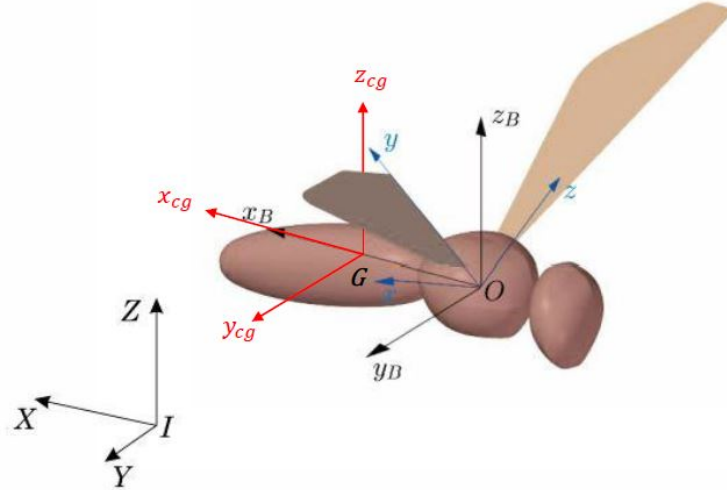
Figure 2.3: Our project reference frames. (1) Inertial reference frame located at an arbitrary point *I*, (2) body reference frame located at *G* (3) Reference frame at point *O* and (4) right wing reference frame (in blue). Figure adapted from [4].

Now that we have defined the reference frames that are going to be used in the project, let us define the way we move from one reference frame to another.

2.4 Euler angles

In order to define the attitude of a vehicle with respect to a given IRF we can use 3 angles, that define a sequence of rotations around specific axes to get from the IRF to the body reference frame. These angles are the so-called Euler Angles [35].

The sequence starts with a rotation around the Inertial Reference Frame *Z* axis of value ψ, the so-called yaw angle. This results in a new reference frame whose axis are (*X'*,*Y'*,*Z'*), note that $Z' \equiv Z$. It follows a rotation of value θ around axis *Y'*, the so-called pitch angle, which results in a new reference frame: (*X"*,*Y"*,*Z"*), where $Y'' \equiv Y'$. Finally the axes of the reference frame at the center of mass are obtained after a rotation of value ϕ_b, or roll angle, around *X"*. The subscript *b* is used to not confuse this angle with future parameters.

Each reference frame of the sequence can be related to the previous one (or the following one) through a squared orthogonal non-singular matrix, whose determinant is equal to 1. For instance the matrix that defines the first rotation of the sequence, the one after a rotation around the *Z*
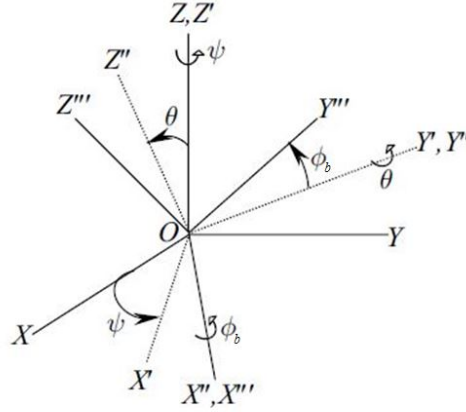
Figure 2.4: Orientations of the body using the Euler angles. Figure adapted from [35]

axis, would be:

$$
\begin{bmatrix} X' \\ Y' \\ Z' \end{bmatrix} = \mathbf{R}(\psi) \cdot \begin{bmatrix} X \\ Y \\ Z \end{bmatrix} = \begin{bmatrix} \cos(\psi) & \sin(\psi) & 0 \\ -\sin(\psi) & \cos(\psi) & 0 \\ 0 & 0 & 1 \end{bmatrix} \cdot \begin{bmatrix} X \\ Y \\ Z \end{bmatrix} \tag{2.8}
$$

Then the orientation of the body reference frame with respect to the IRF can be calculated as:

$$
\begin{bmatrix} x_{cg} \\ y_{cg} \\ z_{cg} \end{bmatrix} = \mathbf{R}(\phi_b) \cdot \mathbf{R}(\theta) \cdot \mathbf{R}(\psi) \cdot \begin{bmatrix} X \\ Y \\ Z \end{bmatrix} \tag{2.9}
$$

Where the rotational matrix that relates both reference frames is:

$$
\mathbf{R}(\phi_b, \theta, \psi) = \mathbf{R}(\phi_b) \cdot \mathbf{R}(\theta) \cdot \mathbf{R}(\psi) \tag{2.10}
$$

2.5 Wing kinematics

The position of an arbitrary point E in the body can be defined as:

$$
\vec{x}_E = \vec{x}_G + \vec{x}_{E/G} \tag{2.11}
$$

If at a given instant of time the angular velocity vector of the body with respect to the IRF is defined as $\vec{\omega}$, the velocity of point E with respect to the IRF at that instant is:

$$
\vec{v}_E = \frac{d\vec{x}_E}{dt} = \vec{v}_G + \frac{d\vec{x}_{E/G}}{dt} + \vec{\omega} \times \vec{x}_{E/G} \tag{2.12}
$$

For a rigid body $\frac{d\vec{x}_{E/G}}{dt} = 0$.

Now that we can define the position and velocity of any point of the body of our model with respect to the IRF, let us define the selected wing kinematics, that will give us the relative position of the wing reference frames w.r.t. the body reference frame.

Both wings are attached to the point O. In this project no heaving movement has been taken into account so $\frac{d\vec{x}_{O/G}}{dt} = 0$. It has also been determined that the orientation of the wings with respect to the body reference frame will be given by 3 angles that are functions of time.

- The angle β defines a rotation around the y_{cg} axis. This rotation is related to the orientation of the stroke plane relative to the body. The reference frame that results from this first rotation is defined as (x_1, y_1, z_1).

$$\begin{bmatrix} x_1 \\ y_1 \\ z_1 \end{bmatrix} = \mathbf{R}(\beta) \begin{bmatrix} x_{cg} \\ y_{cg} \\ z_{cg} \end{bmatrix} = \begin{bmatrix} \cos(\beta) & 0 & -\sin(\beta) \\ 0 & 1 & 0 \\ \sin(\beta) & 0 & \sin(\beta) \end{bmatrix} \begin{bmatrix} x_{cg} \\ y_{cg} \\ z_{cg} \end{bmatrix} \tag{2.13}$$

- The angle ϕ defines the stroke angle, a rotation around the axis x_1 of each wing. Please note that the angle ϕ of the left wing must be the one of the right but with opposite sign, so the movement of both wings is symmetric. The new reference frame is defined as (x_2, y_2, z_2).

$$\begin{bmatrix} x_2 \\ y_2 \\ z_2 \end{bmatrix} = \mathbf{R}(\phi) \begin{bmatrix} x_1 \\ y_1 \\ z_1 \end{bmatrix} = \begin{bmatrix} 1 & 0 & 0 \\ 0 & \cos(\phi) & \sin(\phi) \\ 0 & -\sin(\phi) & \cos(\phi) \end{bmatrix} \begin{bmatrix} x_1 \\ y_1 \\ z_1 \end{bmatrix} \tag{2.14}$$

- The angle α defines the geometric pitching of the wing, a rotation around the axis $y_2 \equiv y_w$, which finally gives the wing reference frame.

$$\begin{bmatrix} x_w \\ y_w \\ z_w \end{bmatrix} = \mathbf{R}(\alpha) \begin{bmatrix} x_2 \\ y_2 \\ z_2 \end{bmatrix} = \begin{bmatrix} \cos(\alpha) & 0 & -\sin(\alpha) \\ 0 & 1 & 0 \\ \sin(\alpha) & 0 & \sin(\alpha) \end{bmatrix} \begin{bmatrix} x_2 \\ y_2 \\ z_2 \end{bmatrix} \tag{2.15}$$

The stroke plane of our insect in the IRF is given by the angle β_{IRF}, that is calculated as: $\beta_{IRF} = \beta + \theta$, figure (2.6).

Thus the rotational matrix that relates the center of gravity reference frame with the wing one is:

$$\mathbf{R}(\alpha, \phi, \beta) = \mathbf{R}(\alpha) \cdot \mathbf{R}(\phi) \cdot \mathbf{R}(\beta) \tag{2.16}$$

As we mentioned earlier, the three angles are functions with time. Let f be the flapping frequency of the wings in Hz, the angles for this project have been defined as:

$$\beta = \beta_m + \beta_0 \sin(2\pi f \cdot t + \Delta\beta) \tag{2.17}$$

$$\phi = \phi_0 \sin(2\pi f \cdot t) \tag{2.18}$$

$$\alpha = \alpha_0 \sin(2\pi f \cdot t + \Delta\alpha) \tag{2.19}$$

Here ϕ_0, α_0 and β_0 are the amplitude of the stroke angle, geometric pitching angle, and stroke plane angle respectively. The parameter β_m is the mean stroke plane angle, and $\Delta\alpha$ and $\Delta\beta$ the phase shift of angles β and α. The two latter parameters are fixed and equal to $90°$.

Such a definition of the angles allows to obtain an analytical expression of the angular velocity $\vec{\omega}_w$ of any of the wing reference frames with respect to the body one, at each instant of time. Please remember that the stroke angle ϕ will be of opposite sign for both wings, an so will be its associated angular velocity.

$$\vec{\omega}_w = \frac{d\beta}{dt} \cdot e_{y_1} + \frac{d\phi}{dt} \cdot e_{x_2} + \frac{d\alpha}{dt} \cdot e_{y_w} \tag{2.20}$$

Where e_{a_b} refers to the unitary vector of axis a of the b reference frame. The unitary vectors can be transformed from their respective reference frames to a selected one, in order to obtain the angular velocity components of the wings in the same reference frame. For instance, the components of the angular velocity vector in the wing reference frame ($\vec{\omega}_w = [p_w, q_w, r_w]$) are:

$$p_w = \dot{\phi}\cos(\alpha) + \dot{\beta}\sin(\phi)\sin(\alpha) \tag{2.21}$$

$$q_w = \dot{\alpha} + \dot{\beta}\cos(\phi) \tag{2.22}$$

$$r_w = \dot{\phi}\sin(\alpha) - \dot{\beta}\sin(\phi)\cos(\alpha) \tag{2.23}$$

Now that we have defined the angular velocity that relates the body axis with the wing ones $\vec{\omega}_w$, the velocity of any point of the wing can be calculated. Taking equations: (2.11) and (2.12) the position of a point P in the wing, with respect to the IRF, is given as:

$$\vec{x}_P = \vec{x}_G + \vec{x}_{O/G} + \vec{x}_{P/O} \tag{2.24}$$

Where $\vec{x}_{P/O}$ represents the relative position vector of P with respect to O. The velocity at point P with respect to the inertial reference frame is then:

$$\vec{v}_P = \vec{v}_O + (\vec{\omega} + \vec{\omega}_w) \times \vec{x}_{P/O} \tag{2.25}$$

Note that the wing has not been designed with any joint, and is assumed to be a rigid surface, thus $\frac{d\vec{x}_{P/O}}{dt} = 0$.

2.5.1 Stroke physical limitations

However the selected definition of the wing kinematics carries a problem. Certain combinations of the angles mentioned above, may cause that the two wings could come in contact with each other, or to even overlap themselves. This would lead to numerical errors and must be prevented forehand. Thus a condition of impermeability between the two wings must be forced, so the stroke amplitude is never bigger than a given threshold ϕ_{max}. As our wings have the origin of their respective reference frames located at the same point O, the threshold must be smaller than 90°.

Figure (2.5) represents the minimum absolute distance between any point of 1 wing with respect to the equivalent one of the other at every instant of the flapping cycle. When this distance is
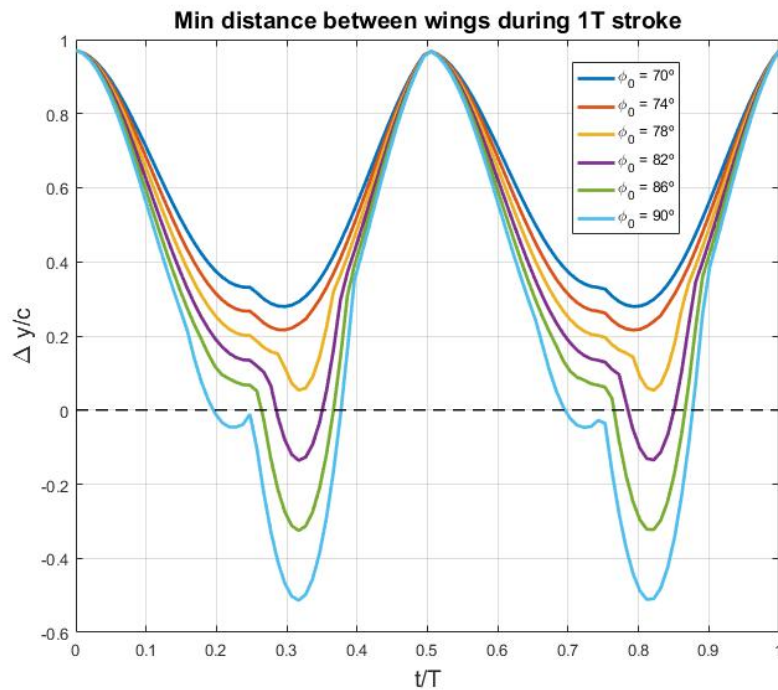
Figure 2.5: Minimum absolute distance between any point of each wing and its equivalent point of the other during a stroke, for a pitching amplitude $\alpha_0 = 70$, and different stroke amplitudes ϕ_0.

0, it means that the two wings have come in contact with each other, and when it is of negative sign means that they have overlap each other. Check that the maximum allowed value of the stroke amplitude for this high geometric pitching amplitude is of about $78°$. That is the selected threshold for this project $\phi_{max} = 78°$.
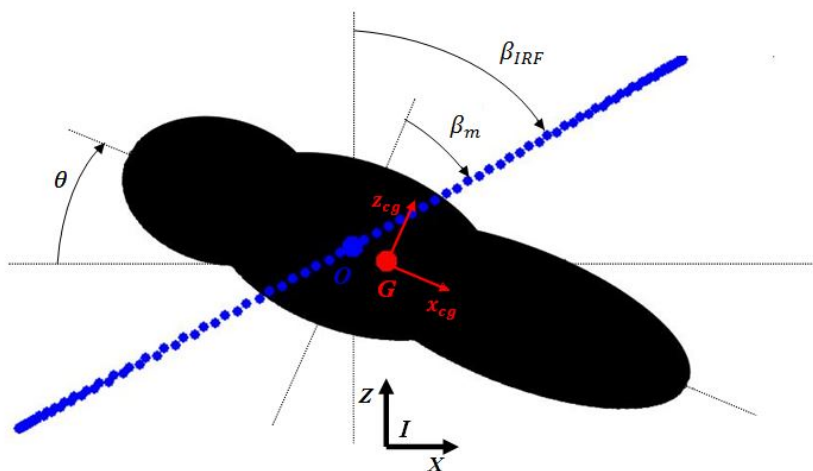
Figure 2.6: Graphical representation of the angles θ, β_m and β_{IRF}. In blue the stroke of the point located at the 75% of the span of the wing, at $x_w = 0$.

Chapter 3

Methodology

In this chapter, we will mathematically describe the problem in hand, together with the proposed strategy to solve it. Some fundamental aspects of the aerodynamic and dynamic models that will be used are also presented.

3.1   Statement of the project

Our problem involves the simulation of the flight of a MAV model during a time $t \in [t_0, t_f]$. As we stated earlier, the objective of the project is to obtain a tool that calculates trimmed flight conditions.

When an air plane performs a straight trimmed forward flight during $t \in [t_0, t_f]$ it needs to move at constant velocity in a giving direction without climbing. From classical mechanics, what this comes to say is that the forces on the aircraft must be in equilibrium at any time. However, in the case of a flapping MAV, the forces on the wings change during the stroke. Thus we cannot guarantee that at every instant of time the resultant forces acting on the vehicle are balanced.

However a trimmed flight condition can be achieved if the movement is periodic, so after a period time $t_f = T = 1/f$, the kinematic characteristics of the model(position, velocity, attitude...) are the same to those at $t = n \cdot T$, where $n = 1, 2, 3...$ [1]

In other words, the final goal of our tool is to select the combination of initial conditions and wing kinematics that result in a periodic flight. With initial conditions we do not only mean the attitude, velocities and position of our MAV, but also the initial conditions of the flow, for they affect the calculation of aerodynamic forces.

The tool must be used on a scheme that gives us the movement of the vehicle during a period for a set of initial conditions. In order to obtain such scheme, two previously developed codes are going to be adapted for this project:

---

[1]Let us make a side note regarding the periodic conditions. For a straight level flight with constant velocity $\pm U_\infty$ in the X direction of the (IRF), the position after a time $t = nT$ must not be equal to that at $t = n \cdot T$, but it must be equal to $X = \pm U_\infty \cdot n \cdot T$, the distance flew by an equivalent point E flying at that constant velocity.

- The **aerodynamic model** of the wings is given by the unsteady vortex lattice method, developed in [4]. The method, not only models the flow over the wings depending on the instantaneous movement of the MAV, but it also defines the wake shed by the wings and its movement.

- The **dynamic model** developed in [25], that integrates the forces calculated by the aerodynamic model, and calculates the resultant movement of the vehicle.

The two models will be briefly explained in following sections. Let us firstly focus on the core of this project, the proposed numerical tool. And to do that we need to gain insight on the mathematics behind it.

3.2 Mathematical problem

In this project we will only focus on the longitudinal behaviour of our MAV, so, instead of using all 6 equations of motion of a rigid body, we will only deal with three:

$$m\frac{d\dot{x}_G}{dt} = \sum F_x \tag{3.1}$$

$$m\frac{d\dot{z}_G}{dt} = \sum F_z \tag{3.2}$$

$$I_y\frac{d\dot{\theta}}{dt} = \sum M_y \tag{3.3}$$

Since no lateral behaviour is considered, at any instant of time $N = L = 0$ and the angular velocity of our body is always: $\vec{\omega} = [0, \dot{\theta}, 0]$, where, θ is the pitch angle of our body. The pitch rate $\dot{\theta}$ will be also referred to as q. Note that $\phi_b = \psi = 0$.

The objective was to find a periodic behaviour for $t \in [0, T]$. This condition means that equations (3.1) to (3.3) must yield:

$$\int_0^T \frac{d\dot{x}_G}{dt}dt = \int_0^T \frac{\sum F_x}{m}dt = 0 \tag{3.4}$$

$$\int_0^T \frac{d\dot{z}_G}{dt}dt = \int_0^T \frac{\sum F_z}{m}dt = 0 \tag{3.5}$$

$$\int_0^T \frac{d\dot{\theta}}{dt}dt = \int_0^T \frac{\sum M_y}{I_y}dt = 0 \tag{3.6}$$

However, the terms $\sum F_x$, $\sum F_z$ and $\sum M_y$ include the aerodynamic forces of the body and the wings, whose value depends on several variables:

$$\sum F_x = f_x(x_G, z_G, \theta, \dot{x}_G, \dot{z}_G, \dot{\theta}, geometry, wing/problem\ kinematics, flow\ characteristics) \tag{3.7}$$

$$\sum F_z = f_z(x_G, z_G, \theta, \dot{x}_G, \dot{z}_G, \dot{\theta}, geometry, wing/problem\ kinematics, flow\ characteristics) \tag{3.8}$$

$$\sum M_y = f_m(x_G, z_G, \theta, \dot{x}_G, \dot{z}_G, \dot{\theta}, geometry, wing/problem\ kinematics, flow\ characteristics) \tag{3.9}$$

This variables can be sorted as follows:

- The **rigid body kinematics** of the MAV: x_G, z_G, θ plus their derivatives.

- The **geometry** of the vehicle which is fixed for $t \in [0, T]$.

- The **wing/problem kinematics**, are those parameters that are fixed at the beginning of each analysis and will not change when $t \in [0, T]$. They have been chosen to be:

  1. f or flapping frequency.

  2. U_∞ and W_∞ that are the aimed constant velocities of the body in the directions X and Z of the IRF respectively.

  3. The parameters that define the kinematics of the wing: β_0, β_m, ϕ_0, α_0. Check that as long as $T = 1/f$ the relative position of the wings wrt the body is the same at $t = 0$ and $t = T$.

- The **flow characteristics**.

Thus $\sum F_x$, $\sum F_z$ and $\sum M_y$ are complex functions with time, that are coupled with variables that are as well functions with time (rigid body/wing/problem kinematics and flow characteristics). The question is whether a given set of initial conditions of the above mentioned variables would lead to a periodic behaviour or not.

Let us define the final set of equations that must be satisfied.

3.2.1   Periodic problem

It has become clear that it would be a tough task to directly determine the right hand side of the nonlinear and coupled equations (3.1) to (3.3). However we can make use of their left hand side:

$$\int_0^T \frac{d\dot{x}_G}{dt} dt = \dot{x}_G(t = T) - \dot{x}_G(t = 0) = 0 \qquad (3.10)$$

$$\int_0^T \frac{d\dot{z}_G}{dt} dt = \dot{z}_G(t = T) - \dot{z}_G(t = 0) = 0 \qquad (3.11)$$

$$\int_0^T \frac{d\dot{\theta}}{dt} dt = \dot{\theta}(t = T) - \dot{\theta}(t = 0) = 0 \qquad (3.12)$$

We also know that an air plane flying a trimmed flight condition, is moving at a constant velocity and attitude: $\dot{x}_G = 0$, $\dot{z}_G = 0$ and $\dot{\theta} = 0$. However we have mentioned that during a flapping cycle, the velocities and pitch rate of the MAV are not constant. So in order to obtain the same attitude and equivalent position, after a period:

$$\int_0^T \frac{dx_G}{dt} dt = \int_0^T dx_G = x_G(t = T) - x_G(t = 0) = U_\infty T \qquad (3.13)$$

$$\int_0^T \frac{dz_G}{dt} dt = \int_0^T dz_G = z_G(t = T) - z_G(t = 0) = W_\infty T \qquad (3.14)$$

$$\int_0^T \frac{d\theta}{dt} dt = \int_0^T d\theta = \theta(t=T) - \theta(t=0) = 0 \tag{3.15}$$

Thus we have 6 kinematic equations that must be fulfilled (from [3.10] to [3.15]). But remember that, among the variables that we identified that were needed in order to calculate the aerodynamic forces, the flow characteristics were also included, and they do change during the time period. So for our solution to be perfectly periodic, these flow characteristics must be equal both at $t=0$ and $t=T$, otherwise the forces after those instants would not be equal and the following movements of the MAV could drift from the periodic conditions.

Residual vector

Let us create a vector $\vec{G}$ whose elements are the above mentioned requirements. The vector will then include, 6 equations related with the kinematics of the body:

$$x_G(t=T) - x_G(t=0) - U_\infty T = 0 \tag{3.16}$$

$$z_G(t=T) - z_G(t=0) - W_\infty T = 0 \tag{3.17}$$

$$\theta(t=T) - \theta(t=0) = 0 \tag{3.18}$$

A quick remark must be done about equation (3.18). Our dynamic model does not model the orientation of the MAV with the use of the Euler angles. Instead, it models the orientation of the vehicle with the use of quaternions Q. The quaternions give the orientation of the model as a rotation about a specific vector, and are presented in following subsections. So instead of one equation (3.18), the 4 components of the quaternion (3 for the vector, 1 for the value of the rotation) must be periodic:

$$Q(t=T) - Q(t=0) = 0 \tag{3.19}$$

$$\dot{x}_G(t=T) - \dot{x}_G(t=0) = 0 \tag{3.20}$$

$$\dot{z}_G(t=T) - \dot{z}_G(t=0) = 0 \tag{3.21}$$

$$\dot{\theta}(t=T) - \dot{\theta}(t=0) = 0 \tag{3.22}$$

Apart from the 9 kinematics relations listed above, we have also mentioned the need to obtain periodic conditions of the flow characteristics. Let all these characteristics be stored in a vector: $\vec{\Psi}$ of dimensions $N_{flow} \times 1$, that includes the characteristics of interest of the given problem. For

instance using a DNS method we may want to include the distribution of velocity or pressure of the fluid domain, while in our case we will focus on the circulation of the wings and the wake, plus the IRF position of the latter. Nevertheless, our finally relation must be:

$$\vec{\Psi}(t=0) - \vec{\Psi}(t=T) = 0 \tag{3.23}$$

The right hand sides of equations (3.16) and (3.17) and from (3.19) to (3.22) plus the N_{flow} right hand sides from (3.23) can be stored in a vector $\vec{G}$, named as the **residual vector** with size $N_G \times 1$:

$$N_G = 9 + N_{flow} \tag{3.24}$$

The vector $\vec{G}$, that is calculated after a period time, will be a function R of a given vector $\vec{q}$, named as the state vector:

$$\vec{G} = R(\vec{q}) \tag{3.25}$$

The elements of the state vector are those variables that must be selected in order to obtain a solution for which $|\vec{G}| = 0$. Let us define what are the selected elements of the state vector.

3.2.2 State vector

As we have stated above, the state vector stores all the variables that will allow us to obtain a residual vector $|\vec{G}| = 0$. Remember that the kinematics of our MAV, are mainly driven by the aerodynamic forces. These forces, as we also reviewed earlier, depended on some fixed wing kinematics parameters, the flow characteristics and the very movement of the vehicle. So as a first approach, we could fix all wing/problem kinematic characteristics and try to obtain the set of initial conditions that allow us to obtain a periodic movement: $x_G(t=0), z_G(t=0), Q(t=0), \dot{x}_G(t=0), \dot{z}_G(t=0), \dot{\theta}(t=0), \vec{\Psi}(t=0)$.

The number of initial conditions is equal to that of the equations to fulfil N_G, so in principle we could use a numerical solver to obtain the combination of initial conditions that satisfy $|\vec{G}| = 0$. However, insects adapt their wing kinematics to reach specific flight condition, and this behaviour is something we will like to imitate in this project. Is there any equation in $\vec{G}$ that could be fulfilled without taking into account its associated initial value?

Initial position of the vehicle

In our models, the flow properties (density, temperature, pressure) and gravity are constant for the whole domain. Thus the solution of our problem must be independent of the selected initial position of our MAV, what we only need to fulfil are the equations (3.16) and (3.17).

Instead of using the initial values $x_G(t=0)$, $z_G(t=0)$ as components of the state vector, we can include two wing kinematics parameters. In this project we chose the mean stroke plane β_m and

the stroke amplitude ϕ_0. The former is related with the direction of the forces of the wings, and the latter to the maximum forces that the two surfaces can generate during the flapping cycle [32].

So the final components of our state vector will be the elements:

$$\beta_m, \phi_0, Q(t=0), \dot{x}_G(t=0), \dot{z}_G(t=0), \dot{\theta}(t=0), \vec{\Psi}(t=0)$$

3.2.3   Newton method

Let us recap. What we have is a vector $\vec{G}$ that is an arbitrary function of a vector $\vec{q}$ and what we need is to select the combination of elements on vector $\vec{q}$ that, for a given set of wing/problem kinematics, yields $|\vec{G}| = 0$.

From an initial state vector $\vec{q}_0$ and its resultant residual vector:

$$\vec{G}(\vec{q}_0) = \vec{G}_0 \tag{3.26}$$

we can define a final state vector:

$$\vec{q}_f = \vec{q}_0 + \Delta\vec{q} \tag{3.27}$$

that yields:

$$\vec{G}(\vec{q}_f) = \vec{G}(\vec{q}_0 + \Delta\vec{q}) = 0 \tag{3.28}$$

If we use a Taylor expansion on $\vec{G}(\vec{q}_f)$, and neglect any derivatives whose order is greater than one we obtain:

$$\vec{G}(\vec{q}_f) = \vec{G}_0 + \mathbf{J} \cdot (\vec{q}_f - \vec{q}_0) \tag{3.29}$$

Where $\mathbf{J}$ is the Jacobian of vector $\vec{G}$ with respect to $\vec{q}$. The Jacobian is a $N_G \times N_G$ matrix whose rows are the derivatives of the elements of $\vec{G}$ with respect to the elements of $\vec{q}$. By imposing $\vec{G}(\vec{q}_f) = 0$ we can rearrange equation (3.29) as:

$$\Delta\vec{q} = -\mathbf{J}^{-1} \cdot \vec{G}_0 \tag{3.30}$$

What we have derived are the basic concepts to define a Newton-Raphsod numerical method. This method starts with an initial guess of $\vec{q}_0$ and its associated $\vec{G}_0$, then calculates the Jacobian matrix numerically and computes $\vec{q}_f$. If the magnitude of $\vec{G}(\vec{q}_f)$ is not equal to 0, but smaller than the magnitude of $\vec{G}_0$; $\vec{q}_0$ and $\vec{G}_0$ are updated as $\vec{q}_f$ and $\vec{G}(\vec{q}_f)$ respectively, and the process is repeated until, after a number of iterations, the magnitude of the residual vector is finally equal or close to 0.

After an iteration k of the Newton method, the new vector would be calculated as:

$$\vec{q}_k = \vec{q}_{k-1} + \Delta\vec{q} \tag{3.31}$$

But what if $|\vec{G}(\vec{q}_k)| > |\vec{G}(\vec{q}_{k-1})|$? In order to try to avoid this result, instead of directly using equation (3.31) to calculate the new state vector, let us calculate $\vec{q}_k$ as:

$$\vec{q}_k = \vec{q}_{k-1} + \gamma \cdot \Delta\vec{q} \tag{3.32}$$

Here γ is a dynamic scalar factor that at each iteration starts with a given value γ_0, which is used to calculate a first $\vec{q}_k$. Then the numerical scheme checks if $|\vec{G}(\vec{q}_k)| < |\vec{G}(\vec{q}_{k-1})|$. If this is not obtained, $\vec{q}_k$ is recalculated with equation (3.32), but this time with a smaller value of γ. This process is repeated until $|\vec{G}(\vec{q}_k)| < |\vec{G}(\vec{q}_{k-1})|$ or γ is reduced up to a determined threshold γ_{min}.

By including this procedure in our numerical method, we may increase the computational time during each iteration, but at least we help the model to converge faster, or even to exit the simulation when it does not seem to converge.

On each iteration we must calculate all the elements of matrix $\mathbf{J}$, which involves at least N_G^2 calculations per iteration. For a big residual vector, like the one we are handling, the computation time becomes too high to fulfil one of our objectives, to obtain a fast tool. Thus another alternative has been considered for this project.

The GMRES method, as it will be explained in more detail in following sections, does not need the value of all elements of $\mathbf{J}$ during each iteration. The method only needs an expression that gives the value of the product of $\mathbf{J}$ times any arbitrary vector with dimensions $N_G \times 1$, which is faster to compute than the whole matrix.

To obtain such an expression, let us revisit equation : (3.29). If we call $\vec{q}_f = \vec{q}_0 + \varepsilon\vec{p}$ where ε is a small scalar value, and $\vec{p}$ the arbitrary vector:

$$\vec{G}(\vec{q}_0 + \varepsilon \cdot \vec{p}) = \vec{G}_0 + \mathbf{J} \cdot \varepsilon\vec{p} \tag{3.33}$$

$$\mathbf{J} \cdot \vec{p} = \frac{\vec{G}(\vec{q}_0 + \varepsilon \cdot \vec{p}) - \vec{G}_0}{\varepsilon} \tag{3.34}$$

Equation (3.34) gives the fundamental function that the GMRES method needs.

The method builds small subspaces of the whole problem (Krylov subspaces), and looks for the equivalent vector of the smaller subspace that reduces the residual of that subspace. In plain words it operates in an equivalent problem of a much smaller size. By repeating these in several subspaces, the method tries to reduce the residual of the complete problem.

3.3   Final numerical tool

Our final numerical tool takes into account all the above mentioned mathematics. Its required inputs are:

- Parameters of the GMRES: maximum allowed size of the Krylov subspace $k_{GMRES_{max}}$, and maximum allowed magnitude of the residual of the subspace err_{GMRES}.

- Parameters of the Newton method: value of ε, maximum number of iterations k_{max}, maximum allowed residual err, initial and minimum values of γ, γ_0 and γ_{min}.

- Initial guess of $\vec{q}$, $\vec{q}_0$ and its associated residual vector $\vec{G}_0$.

Find a comprehensive flowchart in figure (3.3). The final algorithm works as follows:

1. Calculate $\vec{q}_0$ and its associated residual $\vec{G}_0$. Bare in mind that if the initial guess is as similar as possible to the final solution the computation time can be greatly reduced, see Appendix (A).

2. Define equation (3.34).

3. Start the iteration of the Newton method:

   (a) Calculate new $\Delta \vec{q}$ using the GMRES method.

   (b) Check that the calculated stroke amplitude yields: $\phi \leq \phi_{max}$, remember the limitation explained in section (2.5.1).

   (c) Compute new $\vec{q}$ and adjust γ until $|\vec{G}(\vec{q}_k)| < |\vec{G}(\vec{q}_{k-1})|$ or $\gamma < \gamma_{min}$

   (d) Iterate until either the maximum number of iterations k_{max} or the maximum allowed residual err are reached.

3.4   Some notes on the aerodynamic model
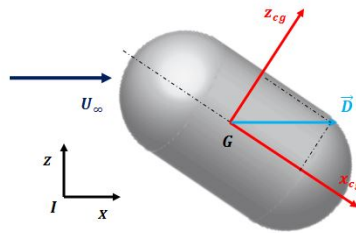
Figure 3.1: 2-D representation of the body as a cylinder and the resultant drag at G.

Although we have already mentioned some of its characteristics, let us introduce the aerodynamic model that will give us the aerodynamic forces that drive the movement of the MAV. The model can be split on the forces produced by the body, and the ones produced by the wings.

3.4.1 Body

Among all the possible aerodynamic effects of the body, the only force that is going to be modelled is its associated parasitic drag, that will act directly on G, figure (3.1). The parasitic drag of the body represents the flow resistance to the movement of the vehicle, and it is, together with the weight of the MAV, one of the forces that the MAV must overcome in order to move in a given direction. The interaction of the body with the wake is also neglected.

The usual expression for the drag depends on the dynamic pressure, cross sectional area of the body and drag coefficient. The magnitude of the drag is defined as:

$$D = \frac{1}{2}\rho v_G^2 S_{body} C_D \tag{3.35}$$

The body was idealised as a cylinder with rounded extremes, so the selected reference area S_{body} and drag coefficient C_D will depend on the attitude of the vehicle.

The components of the drag vector in body axis are calculated depending on the axis selected. For axes y_{cg} and z_{cg} the reference area was set equal to the conservative value:

$$S_{body_{y,z}} = 2 \cdot D_{body} \cdot L_{body} \tag{3.36}$$

On the other hand, for axis x_{cg} the reference area is set as:

$$S_{body_x} = \frac{\pi}{4} D_{body}^2 \tag{3.37}$$

For $j = x, y, z$, the drag components in the body axis are calculated as:

$$(D_j)_{cg} = -\frac{1}{2}\rho \left|\vec{v}_G\right|^2 S_{body_j} C_{D_j} \frac{\vec{v}_G \cdot \vec{e}_{j_{cg}}}{|\vec{v}_G|} \tag{3.38}$$

Where $\vec{e}_{j_{cg}}$ is the unitary vector of axis j of the body reference frame.

As it will be shown later, the Reynolds number of the problem will have a value of around 10^2. In those conditions, the drag coefficient of a cylinder embedded in a cross flow has a value close to unity, [37]. Thus, the drag coefficient for axis, y_{cg} and z_{cg} has been chosen to be equal to:

$$C_{D_y} = C_{D_z} = 1.5 \tag{3.39}$$

When the axis of the body is parallel to the free stream velocity the drag coefficient is assumed to be:

$$C_{D_x} = 0.8 \tag{3.40}$$

The dependance of the drag coefficient on the attitude of running insects was observed by [17], for the case of specimens with similar dimensions to our model.

Thus the body drag mostly depends on the instantaneous velocity of the vehicle and its attitude.

3.4.2 Wings

The wing aerodynamics are calculated using the unsteady vortex lattice method developed in [4]. To gain more insight in the definition of this model, please refer to that project.

From the Navier-Stokes equations, which govern the behaviour of any fluid, the Euler equations can be derived by imposing the conditions:

- Neglect viscosity terms when the *Reynolds* number is much higher than unity: $Re \gg 1$.

- Neglect mass forces when the *Froude* number is much larger than unity: $Fr \gg 1$.

- Neglect heat conductivity, for high Re and Prandtl number $Pr \sim 1$.

- Neglect the effects of chemical and radiation reactions.

Moreover if the flow is also irrotational and incompressible, the velocity of the flow can be expressed as the gradient of a given scalar function, the velocity potential:

$$\vec{V} = \nabla \Phi \tag{3.41}$$

These are the basis that define a potential flow:

$$\nabla^2 \Phi = 0 \tag{3.42}$$

Bare in mind that the forces on each wing depend strongly on the relative flow velocity that they face. The equation that gives the pressure at any position of the potential flow is:

$$\rho \frac{\partial \Phi}{\partial t} + \rho \frac{\|\nabla \Phi\|^2}{2} + p = C(t) \tag{3.43}$$

Equation (3.43) is known as the *Unsteady Bernoulli* equation, where the constant $C(t)$ can be calculated if there is a point in the flow whose velocity and pressure are known. What the equation says is that we do not only need the instantaneous velocity of the flow to calculate the pressure at a given point, but also the variation with time of the velocity potential.

For a wing immersed in a potential flow, the velocity potential at any point can be calculated using the Green's identity. The expression gives the potential at any position of the flow, as a function of the distribution of fluid singularities at the surface of the wing and its wake.

Since these distributions may be difficult to calculate, what a panel method does is to divide the wing and wake in panels, each associated with a constant distribution of a given singularity (i.e. circulation). The circulation is calculated using a boundary condition of impermeability on the wing surface. As the division grows in number of panels, the distribution becomes smoother, and closer to a real scenario.

Our problem is unsteady, the velocity of the wings is changing with time, and this variation changes also the circulation on each wing, and wake panel. In order to tackle this, the problem is solved at given instants of a sampled time $t = 0, \Delta t, 2\Delta t, ...n\Delta t$.

The unsteady panel method developed by [4], divides each wing by N_{wing} panels, i_N chord-wise divisions, j_N span-wise divisions:

$$N_{wing} = i_N \times j_N \tag{3.44}$$

The wake is also divided in panels, and a new row of them is shed from the trailing edge of the wings at each time step. Each panel has a control point located at its 75% chord and it is associated with a vortex ring of constant circulation. The circulation of the panels of the wings are determined at each instant of time, depending on the instantaneous velocity of the vehicle. The value of the time step is equal to:

$$\Delta t = \frac{c/i_N}{4 \cdot U_c} \tag{3.45}$$

Where c is the mean chord of the wing and U_c a characteristic velocity of the problem. In this project the latter has been determined as the product of a characteristic length c times a characteristic angular velocity $2\pi f$.

$$U_c = 2\pi f \cdot c \tag{3.46}$$

Thus Δt roughly represents the time it takes a fluid particle to travel one quarter chord of a wing panel.

Wake model

The method also models the wake, as it plays a role in the calculation of forces on the wings. The wake is divided in N_{wake}:

$$N_{wake} = 2 \cdot j_N \times i_{wake} \tag{3.47}$$

Where i_{wake} is the number of chordwise wake panels. At each instant of time a new row of wake panels is shed from the trailing edge of the wings. From the *Kutta* condition, the circulation of the new row of wake panels is equal to the instantaneous circulation of the panels at the trailing edge of the wings [21].

The wake panels are free to move at each step of time, and from what we have said until now, we could store as many rows of wake panels as we wanted to. However, the effect of a vortex ring at a given point decreases with the distance, and in a real case scenario, the circulation dissipates over time due to viscosity effects. To model these issues, the wake is kept from growing when a given chordwise number of rows of wake panels $i_{wake_{max}}$ is reached.

To sum up, our MAV starts flapping its wing and after each time step, Δt, it sheds a row of wake panels that are free to move in the following time steps. The wake panels are stored in a given matrix that grows in size until the number of stored chordwise rows reaches $i_{wake} = i_{wake_{max}}$. Then the model starts adding the new row of wake panels at each time step by deleting the oldest one.

Residual vector, state vector and flow characteristics

Remember that, when we identified the components of the residual vector $\vec{G}$, we included N_{flow} equations that defined the periodicity of the flow. Now we can finally give name to these flow characteristics, as we were referring to the wake panels position and wing/wake panels circulation.

Remember that equation (3.43) stated that, in order to calculate the forces at $t = 0$ at a given point, we needed to know the variation of the velocity potential at that point with time. If the circulation of the wings and wake panels represent the velocity potential of the flow, we need to store them in our vector $\vec{\Psi}$.

Our vector $\vec{\Psi}$ will then include: the elements of three vectors with the IRF position of all panels of the wake ($\vec{X}_{wake}$, $\vec{Y}_{wake}$, $\vec{Z}_{wake}$) and the elements of two vectors with the circulation of wings and wake panels ($\vec{\Gamma}_{wing}$ and $\vec{\Gamma}_{wake}$). The number of variables we will be dealing with will be:

$$N_G = 9 + N_{flow} = 9 + 2 \cdot N_{wing} + N_{wake} = 9 + j_N \cdot (2 \cdot i_N + i_{wake_{max}}) \tag{3.48}$$

Bare in mind that the initial wake must be a fully developed one, so at $t = 0$, $i_{wake} = i_{wake_{max}}$.

Some comments on the wing forces

From classical aerodynamics we know that the wing forces are not usually perpendicular to the surface of the wing. However, for the case of a flapping vehicle with the characteristics of our MAV, it has been found that, during a flapping stroke there is a leading edge vortex (LEV) attached to the upper surface of each wing [11]. Due to the presence of this LEV, the forces are assumed to be always perfectly normal to the surface. Moreover the induced drag, which is a consequence of the usual tilting of the forces, is also neglected.
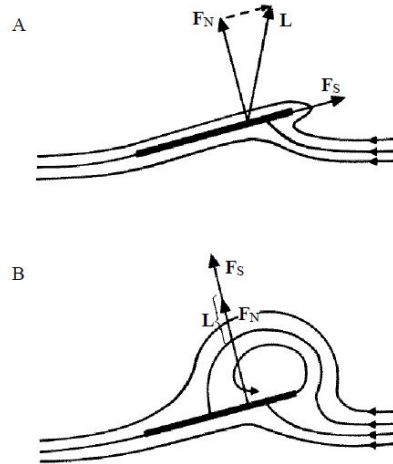
Figure 3.2: (A) represents the orientation of the aerodynamic forces for a thin wing as it is usually calculated for an incoming flow. Here F_s stands for the suction force, a tangential force to the surface. (B) represents the direction of the forces, for a thin wing with a LEV attached to its upper surface. Adapted from [11]

All drag terms related with the wings are neglected, including the parasitic drag of the wings that is also set equal to 0.

These issues have been taken into account when calculating the wing forces.

3.5 Some notes on the dynamic model

We have also mentioned that the dynamic model has been adapted from the one developed in [25]. Please refer to that project to get the whole picture of the model.

The dynamic model calculates the resultant movement of the vehicle after the aerodynamic forces and moments, and the weight of the vehicle are integrated. So at each time step (remember the definition of Δt) the body kinematics of the MAV are calculated with the use of the forces of the previous instant. Needless is to say that this kinematics will then affect the calculation of forces and so on.

It must be noted that, as it was discussed above, the model, instead of using the Euler angles to determine the attitude of the vehicle, uses quaternions. This mathematical representation is free from the singularities that are related with the Euler angles and rotational matrices.

3.5.1 Quaternions

Quaternions are to three dimensions, what complex numbers are to two dimensions, a method to represent orientation. They are derived from the Euler axis/principal angle representation and defined as four mutually dependant scalar values [35]. The first three can be understood as the elements of the unitary vector that is parallel to the instantaneous axis around which the body is rotating. The fourth element is related to the value of the angle that the body will rotate:

$$Q = (\vec{Q}, Q_4) \tag{3.49}$$

$$\vec{Q} = \begin{bmatrix} Q_1 \\ Q_2 \\ Q_3 \end{bmatrix} \tag{3.50}$$

Then the elements of vector $\vec{Q}$ are the components in x, y and z directions.

$$Q_1 = e_x sin(\varphi/2) \tag{3.51}$$

$$Q_2 = e_y sin(\varphi/2) \tag{3.52}$$

$$Q_3 = e_x sin(\varphi/2) \tag{3.53}$$

$$Q_4 = cos(\varphi/2) \tag{3.54}$$

Here φ refers to the angle the body rotates around the axis defined with $\vec{Q}$.

The magnitude of the quaternion must always be equal to 1. Moreover a quaternion can be calculated from a rotational matrix and the other way around, a rotational matrix can be calculated

from a quaternion. There are several subroutines that can perform both calculations, like those included in [35].

3.6 Some notes on the GMRES method

Find in this section, more details of the GMRES method. The method, as exposed earlier, makes use of the concept of the Krylov subspaces and the Arnoldi iteration [15].

3.6.1 Krylov subspaces

For a high order linear system defined as:

$$\mathbf{A}_{n \times n} \cdot \vec{x}_{n \times 1} = \vec{b}_{n \times 1} \tag{3.55}$$

The Krylov subspace theory states that we can create a subspace by using the elements of equation (3.55). The goal is to, instead of working on the original high order problem of size n we can work in a subspace of lower dimension. Let $\vec{x}_0$ be an initial guess of $\vec{x}$, and $m < n$ the size of the Krylov subspace K_m:

$$K_m(\vec{x}_{0_{n \times 1}}, \mathbf{A}_{n \times n}) = span\left\{\vec{x}_0, \mathbf{A}\vec{x}_0, ..., \mathbf{A}^{m-1}\vec{x}_0\right\} \tag{3.56}$$

3.6.2 Arnoldi iteration

The basis that results from the expression (3.56) is a rather messy one. It would be more convenient to work with an orthonormal basis of that subspace instead.

The Arnoldi iteration computes the orthonormal basis from a Krylov subspace of order $m + 1$ using a modified Gram-Schmidt method. The final set of orthonormal vectors $\vec{e}_i$ yields:

$$span\left\{\vec{x}_0, \mathbf{A}\vec{x}_0, ..., \mathbf{A}^m\vec{x}_0\right\} = span\left\{\vec{e}_1, \vec{e}_2, ..., \vec{e}_{m+1}\right\} \tag{3.57}$$

The method looks for a relation between matrix $\mathbf{Q}_{n \times m+1}$, whose columns are $m + 1$ orthonormal vectors $\vec{e}_i$ of size n, matrix $\mathbf{A}_{n \times n}$ and an upper diagonal Hessemberg matrix $\bar{\mathbf{H}}_m$:

$$\mathbf{A}_{n \times n} \cdot \mathbf{Q}_{n \times m} = \mathbf{Q}_{n \times m+1} \cdot \bar{\mathbf{H}}_{m+1 \times m} \tag{3.58}$$

Let $\bar{\vec{e}}_i$ be the orthogonal vector related with the orthonormal vector $\vec{e}_i$. The first vector of the orthonormal basis is obtained as:

$$\vec{e}_1 = \frac{\bar{\vec{e}}_1}{|\bar{\vec{e}}_i|} \tag{3.59}$$

And the following vectors as:

$$\bar{\bar{e}}_{i+1} = \mathbf{A}\vec{e}_i - \sum_{j=1}^{i} \vec{e}_j h_{ji} \tag{3.60}$$

Where h_{ji} is the Gram-Schmidt coefficient , or the value of the normal product between vectors $\vec{e}_j$ and $\mathbf{A}\vec{e}_i$.

$$h_{ji} = [\vec{e}_j]^T \cdot \mathbf{A}\vec{e}_i \tag{3.61}$$

If we also say that:

$$\vec{e}_{i+1} = \frac{\bar{\bar{e}}_{i+1}}{h_{i+1,i}} \tag{3.62}$$

By introducing equations, (3.61) and (3.62) in (3.60), and using some simple algebra, we can finally arrive to the expression:

$$\mathbf{A}\vec{e}_i = \sum_{j=1}^{i+1} \vec{e}_j h_{ji} \tag{3.63}$$

If we orderly store all possible combinations of h_{ji} in a upper diagonal Hessember matrix, the equation (3.63) is equivalent to any of the resultant column equations of the relation (3.58).

3.6.3 GMRES

The GMRES method looks for a solution $\vec{x}_f$ to the problem (3.55) that can be described as:

$$\vec{x}_f = \vec{x}_0 + \mathbf{Q}_m y_m \tag{3.64}$$

Where $\mathbf{Q}_m$ is the matrix $\mathbf{Q}_{n \times m}$ calculated with the use of the Arnoldi iteration, $\mathbf{Q}_{m+1}$ a matrix $\mathbf{Q}_{n \times m+1}$, and y_m a vector of m elements.

For an initial guess $\vec{x}_0$, the associated residual is:

$$\vec{r}_0 = b - \mathbf{A}\vec{x}_0 \tag{3.65}$$

And the objective is to get the residual $\vec{r}_f$ associated to $\vec{x}_f$ that has the smallest magnitude possible:

$$\vec{r}_f = b - \mathbf{A}\vec{x}_f \tag{3.66}$$

In order to obtain that, the GMRES method operates in a Krylov subspace of size $m+1$, calculated as:

$$K_m(\vec{r}_0, \mathbf{A}) = span\left\{\vec{r}_0, \mathbf{A}\vec{r}_0, ..., \mathbf{A}^m\vec{r}_0\right\} \tag{3.67}$$

From which it builds an associated orthonormal basis using the Arnoldi iteration. Let the first element of the basis, $\vec{e}_1$ be calculated as:

$$\vec{r}_0 = \delta\vec{e}_1 = \delta\mathbf{Q}_{m+1}[1, 0, ..0]^T = \delta\mathbf{Q}_{m+1}\vec{u}_1 \tag{3.68}$$

By introducing equation (3.64) in equation (3.69), and using (3.58) we can arrive to the expression:

$$|\vec{r}_f| = |\mathbf{Q}_{m+1}(\delta\vec{u}_1 - \bar{\mathbf{H}}_m\vec{y}_m)| \tag{3.69}$$

Where $\mathbf{Q}_{m+1}$ is of unit order, since it is an orthonormal basis. Thus the final equation to be satisfied is:

$$|\delta\vec{u}_1 - \bar{\mathbf{H}}_m\vec{y}_m| = 0 \tag{3.70}$$

So we need to iterate and build the Krylov subspace until the vector $\vec{y}_m$ reduces the left hand side of equation (3.70) to a given threshold or m, the size of the subspace, reaches a maximum. In our project this maximum size is much smaller than the dimension of the Jacobian so we can guarantee that, on each iteration, the number of calculations performed is much smaller than those of a Newton-Raphsod method.

As long as we can obtain the product of $\mathbf{A}$ times any arbitrary vector, we can calculate the components of $\bar{\mathbf{H}}$ using the Arnoldi iteration. Then by using an initial guess $\vec{x}_0$ and its associated residual, $\vec{r}_0$ we can obtain the vector $\vec{y}_m$ that better approximates equation (3.70). That solution can be converted to our original problem using equation (3.64). If we repeat this sequence for several subspaces, the residual of the whole problem is expected to be reduced.
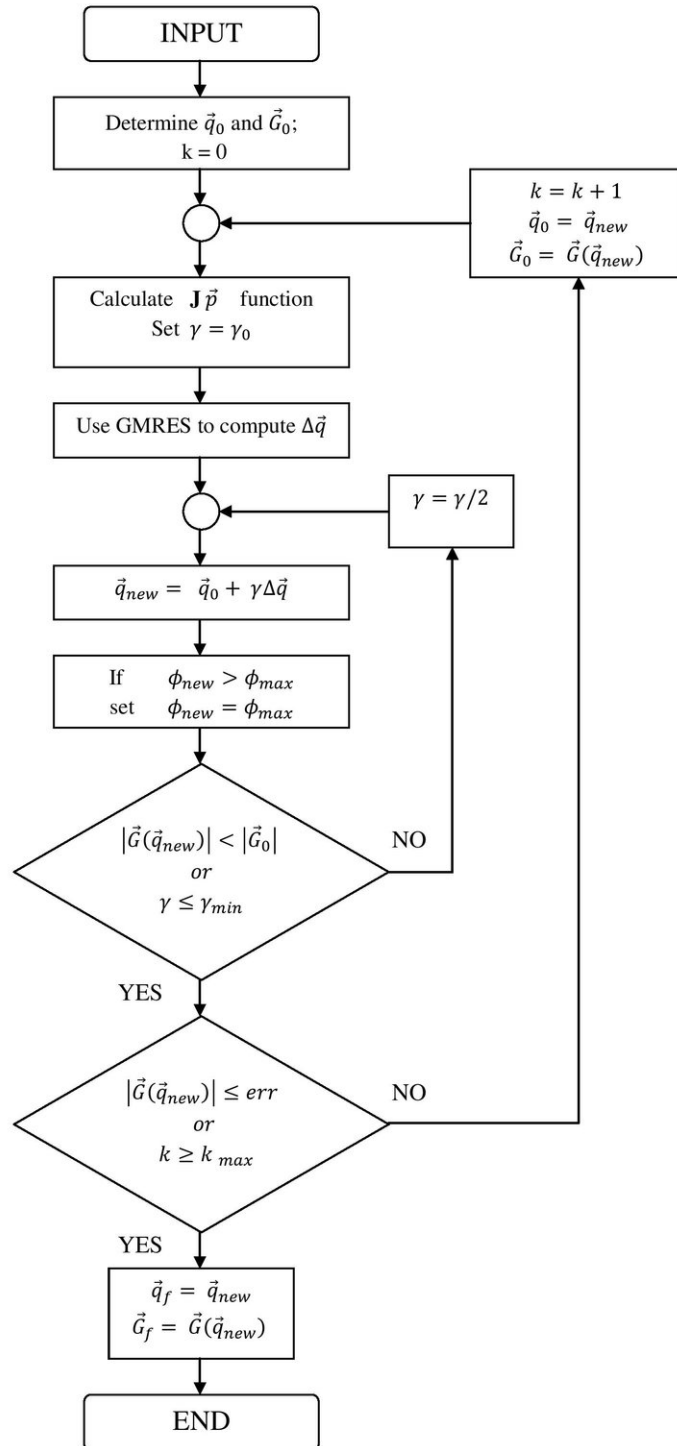
Figure 3.3: Flow chart of the numerical tool

Chapter 4

Results

In this chapter we will present the results of some flight conditions and parameter analyses. But first, let us discuss how we tuned the numerical tool and selected the configuration of wing and wake panels. The configuration will greatly determine the computation time, but also how rigorous our analyses will be.

4.1   Selection of parameters for the numerical method

Apart from the initial guess of the target and residual vectors, we determined some parameters that were used as inputs of the numerical tool. The combination that makes the tool faster may change with each analysis, but here we present some general hints on how to choose it.

- **Newton method**. Most cases required less than 6 iterations to converge. In fact those cases that did not converge before that value usually ended up diverging. We recommend a value of $k_{max} = 15$ in order to be conservative. Regarding the parameter err, for a non-dimensional residual vector, a magnitude of 10^{-4} was expected to be as good as it could get. Regarding the small scalar value ε it was set equal to 10^{-7}. The initial γ was set equal to $\gamma_0 = 1$, and the minimum allowable one $\gamma_{min} = 10^{-2}$. For smaller values than that the problem is not expected to get better at each iteration.

- **GMRES method**. The GMRES method also requires a maximum number of iterations $k_{GMRES_{max}}$ (maximum size of the Krylov subspace) and a maximum allowable magnitude of the residual vector of that subspace err_{GMRES}. The former was chosen so the size of the subspace was much smaller than that of the whole problem n, and bigger than the number of kinematic relations to be yielded. A value $k_{GMRES_{max}} = 30\%n$ was found to be fast and conservative. The maximum allowable magnitude of the residual was set at least one order of magnitude smaller than the parameter err, so the residual in that subspace can not be bigger that what we want to impose on the whole problem.

4.2 Grid resolution

In order to calculate the forces that resulted from different configurations of wing and wake panels, an initial rather simple forward flight analysis named as the *case zero* was performed with $i_N = 2$, $j_N = 3$ wing panels divisions and $i_{wake_{max}} = T/\Delta t$ wake chord-wise panels. The resultant periodic movement was saved, and used to perform the sensitivity analyses on the distribution of wing and wake panels. Our objective was to find the best cost-effective distribution.

4.2.1 Wake panels

The number of wake panels selected will affect the calculation of the aerodynamic forces, so it is expected that, as the number of panels increases, the forces become smoother and more similar to an equivalent real case. However, as we increase their number, our state vector grows in size by a factor N_{wake}^4. By fixing the configuration of wing panels $N_{wing} = i_N \times j_N = 2 \times 3$, we varied the parameter $i_{wake_{max}}$, that was calculated as:

$$i_{wake_{max}} = n \cdot \frac{T}{\Delta t} \tag{4.1}$$

Where n was equal to: $n = 1, 2, 3, 4, 5, 6$. For each wake panels case, the MAV was forced to move $n + 4$ periods repeating the movement obtained after *case zero*. Then the forces during the last two periods of each case were compared with the forces of the case $n = 6$, the case that had more wake panels.
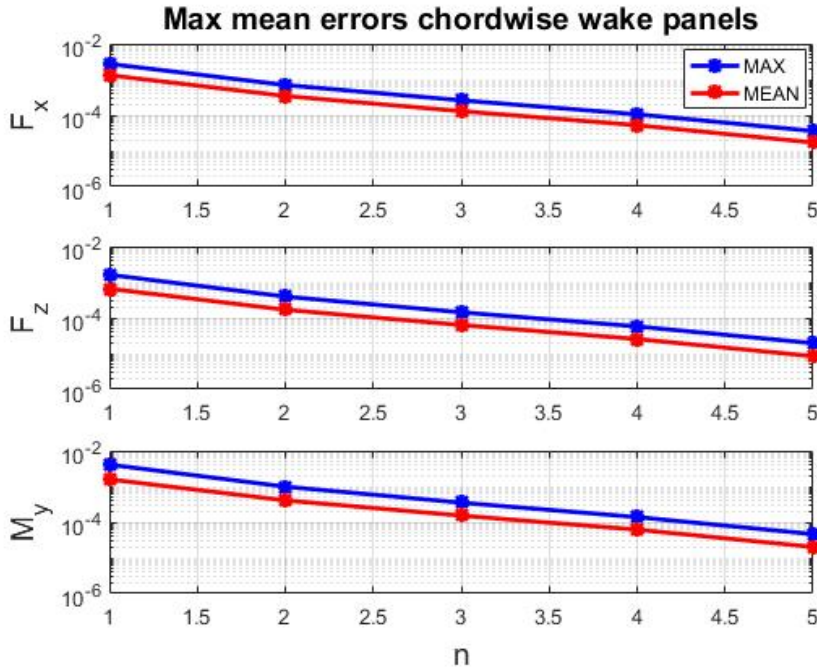
Figure 4.1: Max and mean errors of the wing forces in body axis during 2 flapping cycles of forward flight for different $i_{wake_{max}} = n \cdot \frac{T}{\Delta t}$ cases with respect to the case for $n = 6$.

From figure (4.1) the maximum and mean errors for $n = 1$ with respect to $n = 6$ are not that high given that the computation time is the smallest for the $n = 1$ case. Thus the final $i_{wake_{max}}$ was determined to be $i_{wake_{max}} = T/\Delta t$.

4.2.2 Wing panels

As it was discussed earlier, the division of the wings in panels ultimately gives the accuracy of the flow on top of these surfaces, and also sets the span-wise divisions of wake panels. Thus it not only affects how rigorous our solution will be, but also the computation time.

By setting the maximum number of chord-wise wake panels equal to $i_{wake_{max}} = T/\Delta t$, the vehicle was forced to move with the calculated movement of the *case zero* analysis, for different wing panels distributions. So starting from $N_{wing} = i_N \times j_N = 2 \times 3$ panels, the chord-wise and span-wise panels are increased by a factor of 2. The computation time, however, will increase by a factor higher than e^4 for each additional analysis, so we will only focus on those cases that are as rigorous and quick as possible.

Apart from the *case zero*, two more analysis were performed, one with $N_{wing} = i_N \times j_N = 4 \times 6$ panels and other with $N_{wing} = i_N \times j_N = 8 \times 12$ panels. The resultant mean and maximum errors of the two first cases, with respect to the last one, are presented below:

	2×3 mean error	4×6 mean errror	2×3 max errror	4×6 max errror
$F_{x_{cg}}$	10.28%	4.95%	35.98%	18.54%
$F_{z_{cg}}$	5.19%	2.46%	12.9%	7.54%
$M_{y_{cg}}$	15.06%	6.81%	45.77%	18.9%

Table 4.1: Mean and maximum errors during 2 flapping cycles between the aerodynamic forces of the wings in body axis for the configurations $N_{wing} = 2 \times 3$ and $N_{wing} = 4 \times 6$, with respect to the case for $N_{wing} = 8 \times 12$.

After discussing the results presented in table (4.1), and taking into account their related simulation times, the most suitable configuration was determined to be the one for $N_{wing} = 4 \times 6$ panels.

4.3 Forward flight

Now that we have defined what our configuration of wing and wake panels is going to be, we can start our analyses of interest. The first flight condition we decided to focus on, was the forward flight of our MAV.

First the fixed parameters related with the wing kinematics, that are not included in the state vector, must be set, remember section (3.2). The parameters were:

- The flapping frequency f which also determines the period of the movement $T = 1/f$. From the literature we know that insects of the order *Dipteria* have frequencies that usually range between $200 - 300$ Hz, [36]. The frequency that was selected was:

$$f = 260 Hz \tag{4.2}$$

- The forward flight velocity U_∞ was set equal to the characteristic velocity of the problem.

$$U_\infty = -U_c = -2\pi \cdot f \cdot cm/s \tag{4.3}$$

- The vertical velocity was set equal to 0:

$$W_\infty = 0m/s \tag{4.4}$$

- The stroke plane amplitude β_0 was also set equal to 0:

$$\beta_0 = 0° \tag{4.5}$$

- And finally the wing geometric pitching amplitude α_0, which will ultimately determine the effective angle of attack of the wings:

$$\alpha_0 = 70° \tag{4.6}$$

The analyses are performed taken into account the standard atmospheric air conditions at sea level. If our characteristic length is the mean chord of our wings the resultant Reynolds number is:

$$Re = \frac{\rho U_c c}{\mu} = 128.412 \tag{4.7}$$

Thus the approximate Reynolds numbers we are going to be working with are of the order: $Re \sim 10^2$.

Secondly we need to initialize our problem, so we calculate an initial guess that includes a fully developed initial distribution of wing and wake panels. Bare in mind that an initial guess of the state vector that is as close as possible to the final solution will greatly reduce the computation time. Find two proposed methods in appendix (A).

Let us call this first analysis our *Nominal case*, and summarize its main results below:

The top plot to the left in figure (4.3) represents the position of the G with respect to an equivalent moving point E with constant IRF velocity $\vec{V}_E = [U_\infty, 0, W_\infty]$. Find indicated the instants of time for pronation (2), supination (3) with red hollow dots; and initial, final position with a filled blue dot. The top plot to the right represents the resultant evolutions of the elevation angle θ and the stroke plane angle with respect to the vertical plane of the IRF $\beta_{IRF} = \theta + \beta$, figure (2.6). The two bottom plots represent the linear velocities and angular velocities of the vehicle. Here q stands for the pitch rate: $q = \dot{\theta}$.

The instants of pronation and supination represent those instants of time at which the relative velocity of the wings with respect to the body are equal to 0. It is at those instants of time when the effects of the flow are expected to play major roles in the calculation of forces in the wings.

In figure (4.4) forces F_x of negative sign represent the thrust that the MAV produces in order to overcome the parasitic drag of the body, and the forces F_z of positive sign represent vertical forces
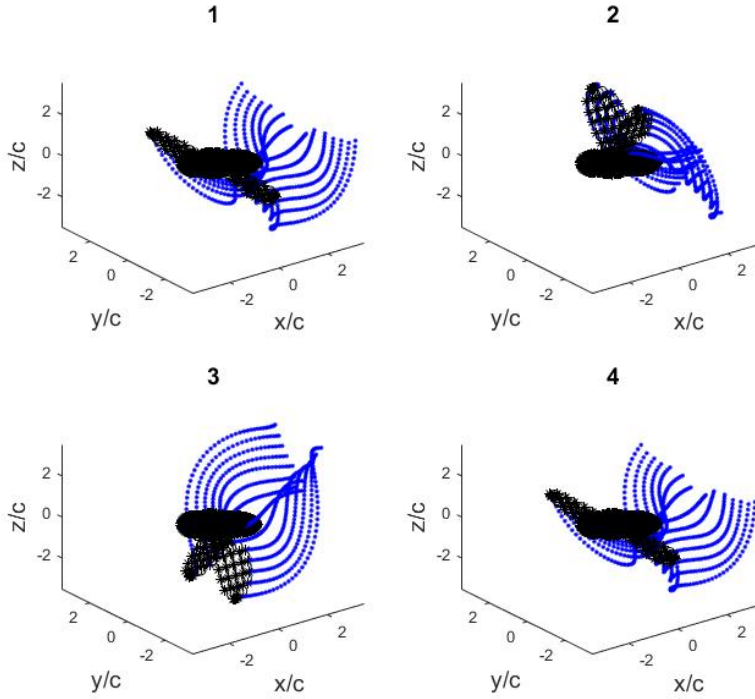
Figure 4.2: Four instants of the flapping cycle during forward flight. In black the MAV body and wing panels; in blue the wake. Initial position (1) $t = 0$, pronation (2), supination (3) and final position (4) $t = T$.

that must counteract the weight. The mean value of the former is of negative sign, and the mean value of the moments produced in the wings is close to 0, which balances the angular equilibrium. However notice that the mean value of the non-dimensional F_z force is also close to 0. Thus the force that is balancing the MAV in that direction must have another source, the parasitic drag of the body.

We calculated the components of this force depending on which direction of the body axis we were in. It turns out that, given that the selected reference areas and drag coefficient in the (y_{cg}, z_{cg}) directions are always much higher than the ones of the axial (x_{cg}) direction, the drag is not always aligned with the free stream velocity, figure 4.27). In fact, for a free stream velocity $U_\infty < 0$ in the X direction of the IRF, for pitch angles bigger than 0, the drag was found to point in the positive X and Z direction.

Thus our wings are mainly focused on providing thrust to counteract the horizontal drag, while it is the body the one in task of providing a big percentage of the required lift to counteract the weight. Of course this is something that is not observed in a real insect. Although the typical body of flying insects are usually shaped in order to enhance the aerodynamic forces, and that, at the high velocities we are performing our analysis, these forces could play a major role, our model surely is unrealistic. Unfortunately this issue was found once all the cases of forward flight were computed. We will present them so we can comment some of their characteristics with respect to a more realistic scenario afterwards.
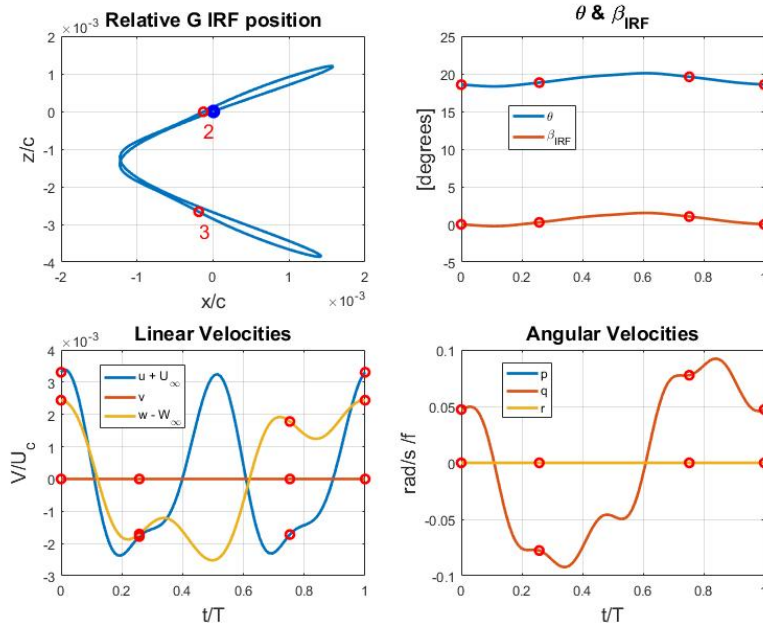
Figure 4.3: One period history of the MAV kinematics in forward flight.
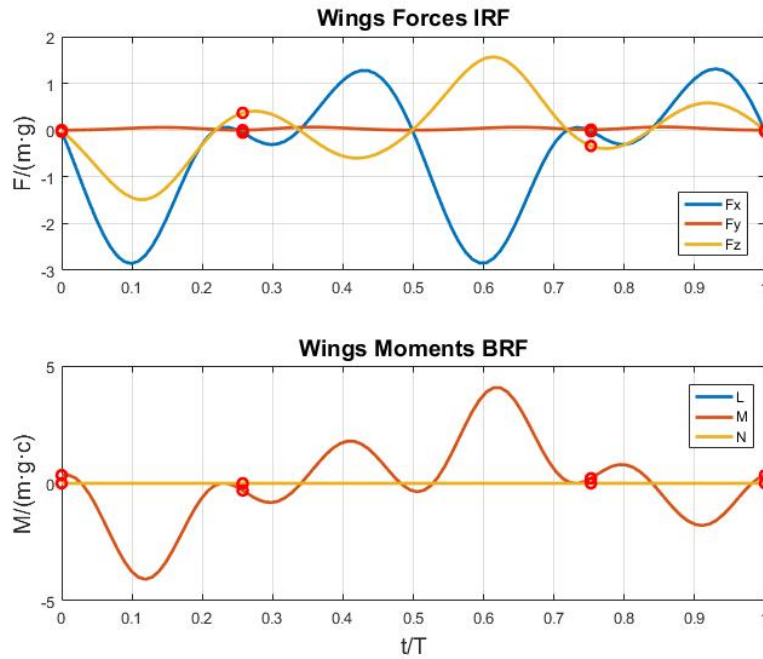
Figure 4.4: One period history of the wing forces (IRF) and moments (body axis) in forward flight.

4.3.1   Robustness analysis

Now that we have a state vector that results in a near periodic movement of the MAV during forward flight, we can also check if that state vector also results in a stable behaviour by letting

the vehicle fly during additional periods. If we find the same velocities and attitude of the MAV at the beginning of each of them, we could conclude that the movement is stable.
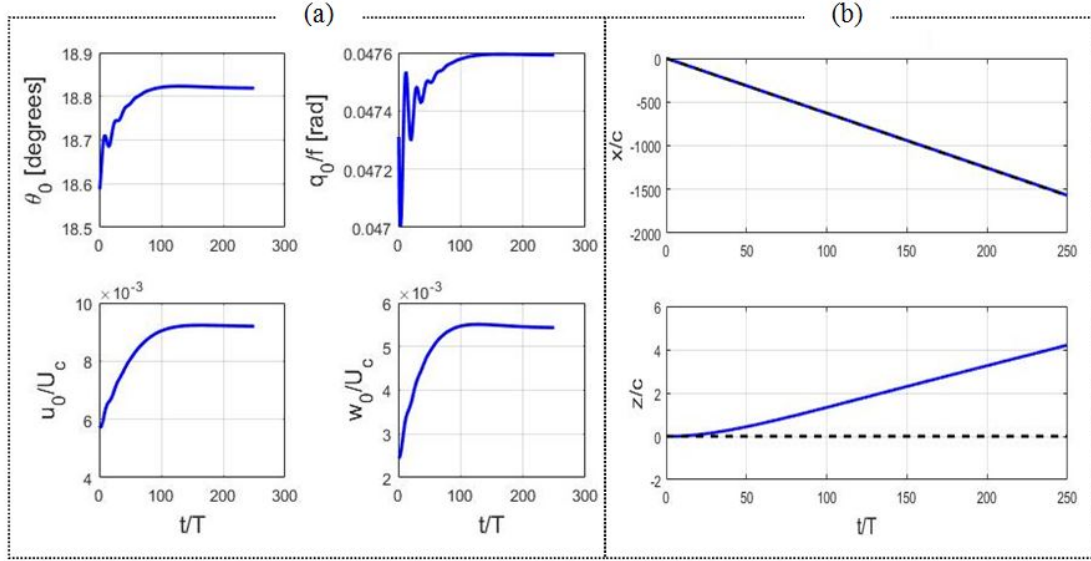
Figure 4.5: Forward flight characteristics of the MAV for $t > T$. Subscript "0" stands for the initial condition at each period (a). (b) Position of G during $t > T$ periods in forward flight.

In figure $(4.5), (a)$ notice that u_0 stands for: $u + U_\infty$ at the begining of each period. Our model does reach a stable forward flight, while most references agree that the flight of a fruit fly is inherently unstable , [23]. But remember, during a stroke the mean value of the wing forces mostly points in the horizontal direction. Moreover the mean value of the moments of the wings and their vertical forces are close to 0. Even if there were an increase of the vertical force, to help counteract the weight, and the MAV tried to increase its pitch angle, the horizontal forces would produce a nose down torque that will counteract it.

So the mean torque applied in the center of mass during the stroke is almost equal to 0, and the drag of the body, that is applied in the very center of mass of the vehicle, counteracts the weight.

Figure $(4.5), (b)$ shows the trajectory of the MAV model in forward flight in blue compared with an equivalent moving point E with constant IRF velocity $\vec{V}_E = [U_\infty, 0, W_\infty]$, in dashed black line. The resultant movement includes a vertical overshoot, that, despite being negligible compared with the horizontal displacement, does not allow the MAV to purely perform straight forward flight.

4.3.2 Off-design performance on flapping frequency and forward flight velocity

One of our objectives was to check what are the effects of changing some parameters of our problem. So, starting from the *nominal case* that we presented above, we varied the value of the forward flight velocity U_∞ and the flapping frequency f and checked what their effects were.

Different researchers have determined that the flapping frequency is not only one of the main parameters related with power consumption, together with the wing stroke amplitude, but they also allow the insect to control its movement [33].

Using the instantaneous velocity and forces on the wings, we could calculate the mean power required to keep the vehicle aloft and the maximum peak of power after a period time.
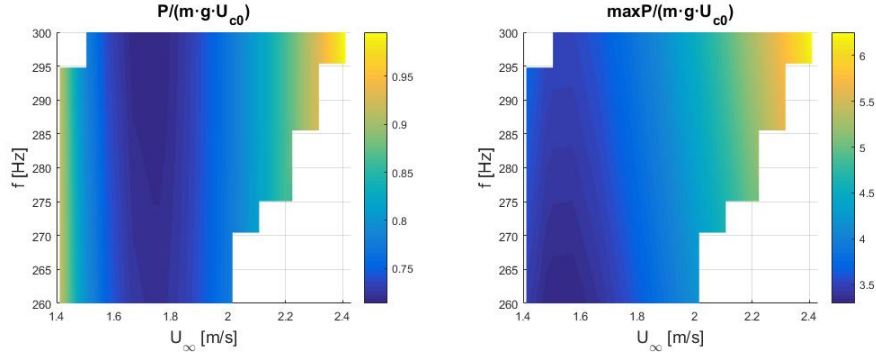
Figure 4.6: Mean consumed power and maximum peak of consumed power during a trimmed flapping forward flight cycle, for different values of flapping frequency and absolute velocity.

Here U_{c0} stands for the characteristic velocity of the nominal case, the one calculated for $f = 260Hz$.

From figure (4.6) it can be deduced that it could be preferable to fly at higher flapping frequencies, as the mean consumed power is reduced. However, by doing so, the maximum peak of consumed power during the flapping cycle would increase. When designing the power source that would ultimately drive the MAV, a compromise should be made between both parameters, so the movement uses the lowest mean power possible that results in the smallest power peaks.

From figure (4.6) it can also be seen that for each flapping frequency, there is a region of forward flight velocities where the power is minimum. It is at those velocities when it seems that our poorly modelled drag force, that until now has been in charge of keeping the vehicle aloft, starts to decrease. Thus the model tries to change its IRF stroke plane so it increases the vertical component of the wing forces. It also tries to increase its stroke amplitude since the wings do not only have to overcome the drag, but also some percentage of the weight, figure (4.7).

Please observe how tight the stroke amplitude is related with the power consumption, as more stroke amplitude means more power. This behaviour corresponds to the way the power is calculated, (as the velocity of the wings times its forces), but it was also observed by [32], with a more comprehensive analysis.

Independently of the flapping frequency we choose, as we increase the forward flight velocity, the model tries to align its body with the free stream velocity. Then the mean stroke plane angle β_m is adjusted so the mean IRF stroke plane is perpendicular to the flying direction. Remember that, as we increase the forward flight velocity, the magnitude of the drag increases as it depends on the velocity to the square. Then, as long as the body forces are able to counteract the weight, the kinematics of the wings are adjusted so more effort is put on increasing the thrust.

We may also be interested on how much do the kinematics of the MAV oscillate during a period
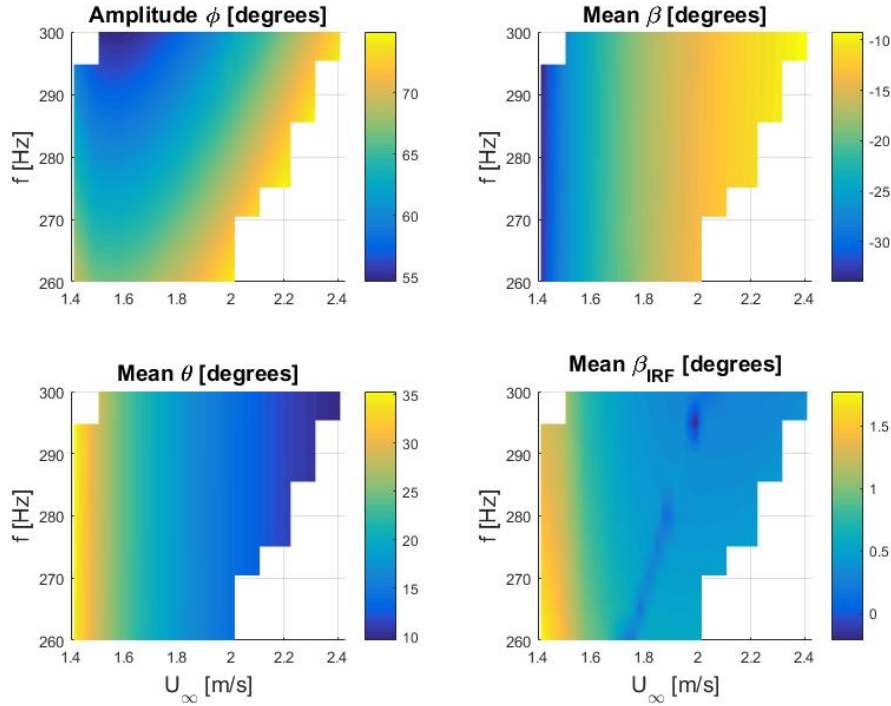
Figure 4.7: Stroke amplitude ϕ_0, mean stroke plane angle β_m, mean elevation angle θ_m and mean IRF stroke plane angle, with respect to different flapping frequencies and forward flight velocities.

time. In order to do that we can calculate the resultant standard deviations of certain parameters. Some of the results are displayed in figure (4.8). In general as we increase the stroke amplitude, ϕ_0, the oscillations increase, as the magnitude of the wing forces increases.

Find in figure (4.8) the standard deviations of the position of the center of mass (x_G, z_G) and its velocities (u,w) G, with respect to an equivalent moving point E with constant IRF velocity $\vec{V}_E = [U_\infty, 0, W_\infty]$. Find at the bottom the standard deviations of the pitch angle and pitch rate of the MAV.

The horizontal parameters, linear velocity u along the IRF X direction and the position x_G, present smaller oscillations as the forward flight velocity is reduced, independently of the frequency. Take into account that, in these conditions, not only the magnitude of the body drag is smaller, but also the component of the wing forces along the X direction are reduced as the orientation of the stroke plane angle (body and IRF) changes.

It can be checked that in figures (4.6), (4.7) and (4.8), there are two velocity limits for each flapping condition up to which the tool was able to obtain trimmed conditions. Both limits are related with the maximum achievable forces of the wings before the stroke amplitude limitation is met. In order to obtain more trimmed flight conditions, such as hover, we may amend this by changing one or some of the fixed wing kinematics parameters.
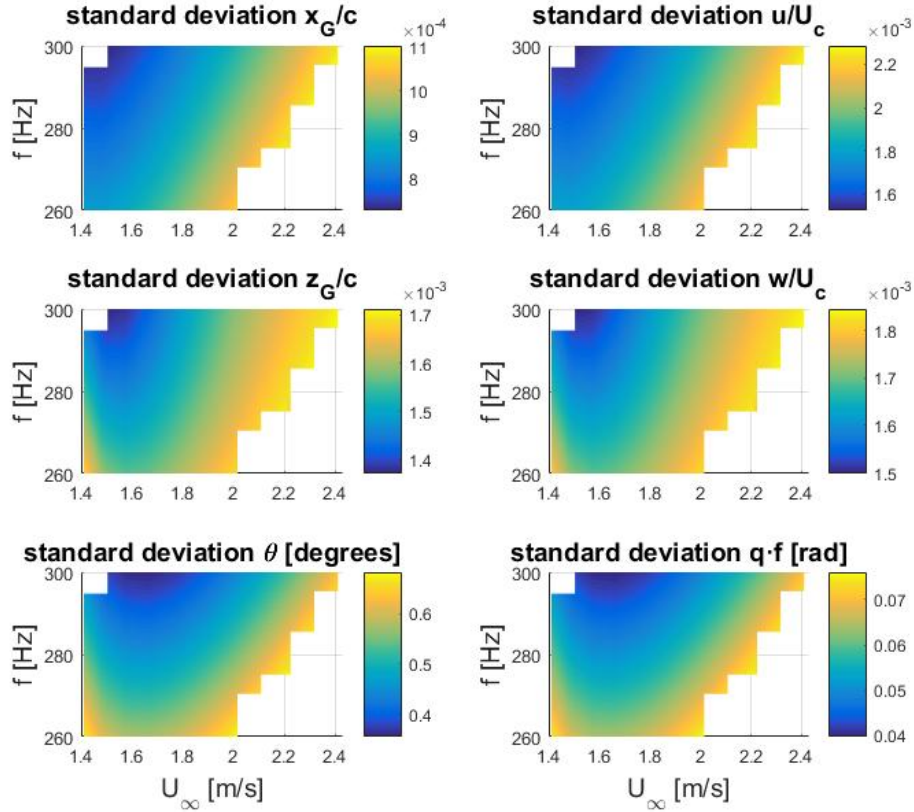
Figure 4.8: Standard deviations of some kinematics of the body, during a period of trimmed forward flight.

4.4 Hover

Previously we have set the values of the fixed parameters that better adjusted to the desired forward flight condition, and one of them was the stroke plane amplitude: β_0. We can find in the literature some real footages of the shape of the stroke of insects performing hover (or hummingbirds) [16, 2, 30]. From these footages it is hinted the need to include a value of β_0 different from 0. By setting this value to $\beta_0 = 15°$, for instance, we were able to find a periodic solution of the hover flight case, where $U_\infty = 0$.

Find in figure (4.10) the position of G with respect to an equivalent point E moving with constant IRF velocity $\vec{V}_E = [U_\infty, 0, W_\infty]$. Find indicated the instants of time for pronation (2), supination (3) with two red hollow dots, and initial; final position with a filled blue dot.

From figure (4.11) the forces in the Z direction produced by the wings are the ones in charge of counteracting the weight of the model. Moreover the mean value of the horizontal forces and wing moments are close to 0. Thus for the case of hover, the unsatisfying drag model does not seem to play any major role.

It must be noted that the configuration of wake and wing panels selected was the same as for the
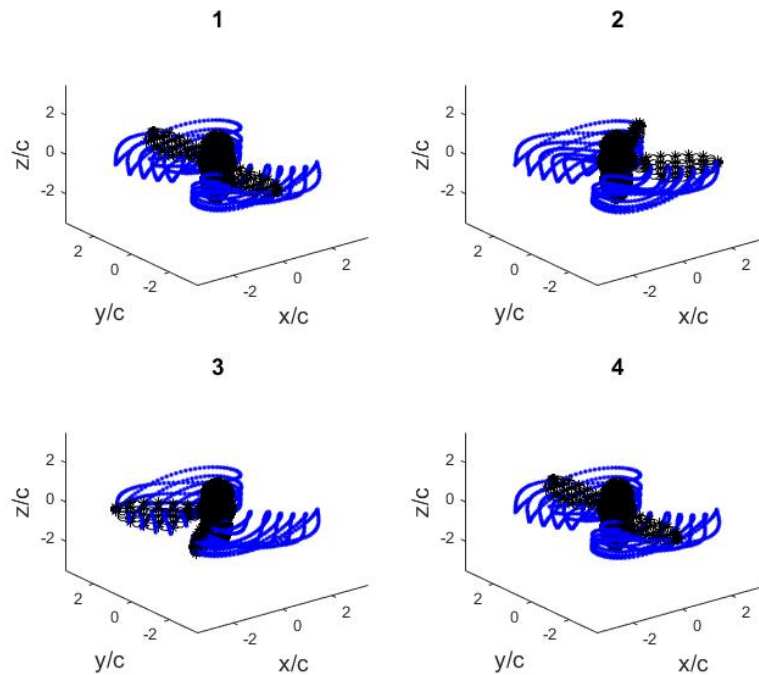
Figure 4.9: Four instants of the flapping cycle during hover. In black the MAV body and wing panels, in blue the wake. Initial position (1) $t = 0$, pronation (2), supination (3) and final position (4) $t = T$.
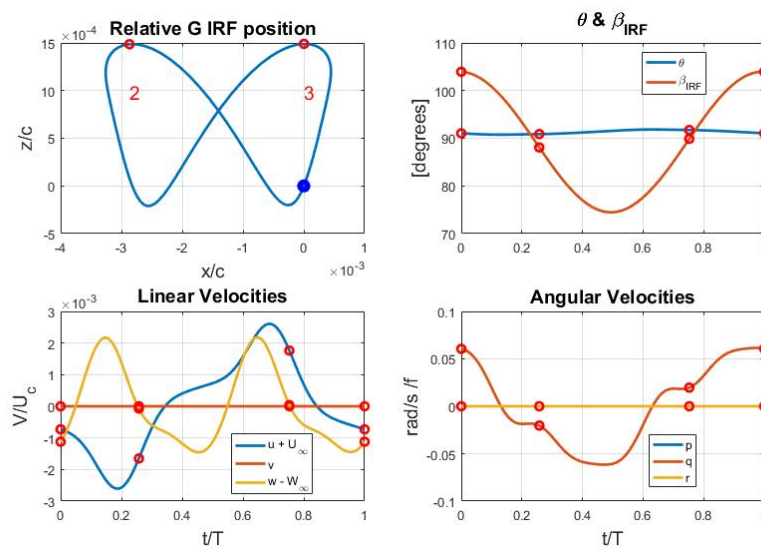
Figure 4.10: Kinematics of the MAV during 1T trimmed hover flight.

forward flight case. However, during hover, the wake remains much closer to the wings (figure (4.9)) that what it did for the case of forward flight (figure (4.2)). A grid study for the case of hover flight has been left for future projects.
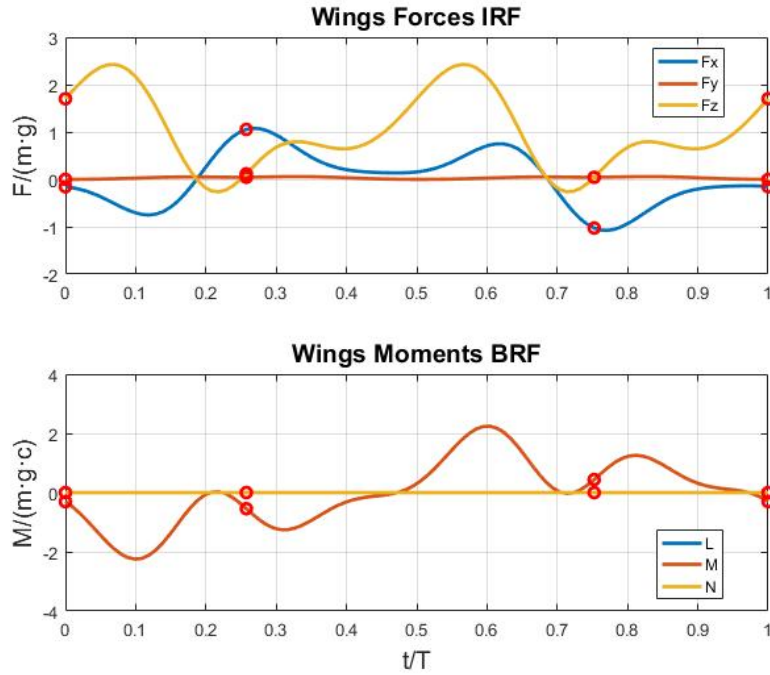
Figure 4.11: One period history of the wing forces (IRF) and moments (body axis) in hover.

4.4.1 Robustness analysis

Now that we have our state vector for hover, we can also study whether it results in a stable flight or not.

Despite our model lacks some important characteristics, like the drag of the wings, that in real life acts as a passive stability feature, our resultant unstable hover (4.12) is similar to the cases found using quasi-steady analyses [31]. In fact there are studies that relate part of the observed unstability of flying insects in hover with the effects of the wake close to the wings [6]. This possibility however has not been analysed in this project, and this task is left for future projects.

Between stability and manoeuvrability, flying insects choose the latter. In order to perform a stable flight, they have developed some mechanisms and systems, like halters [2, 23, 29], that allow them to control they flight.

4.4.2 Off-design performance on the flapping frequency

As we did before for the case of forward flight, we have also performed some analyses on the flapping frequency and its effects in hover.

From figures (4.13) to (4.15), it could be deduced that the best hover condition would correspond to the maximum allowed frequency, as the power and oscillations are minimum for that case. However we should take a step back and remember that we have not taken into account any drag of the wings. Without this additional force, the MAV will always tend to increase its flapping
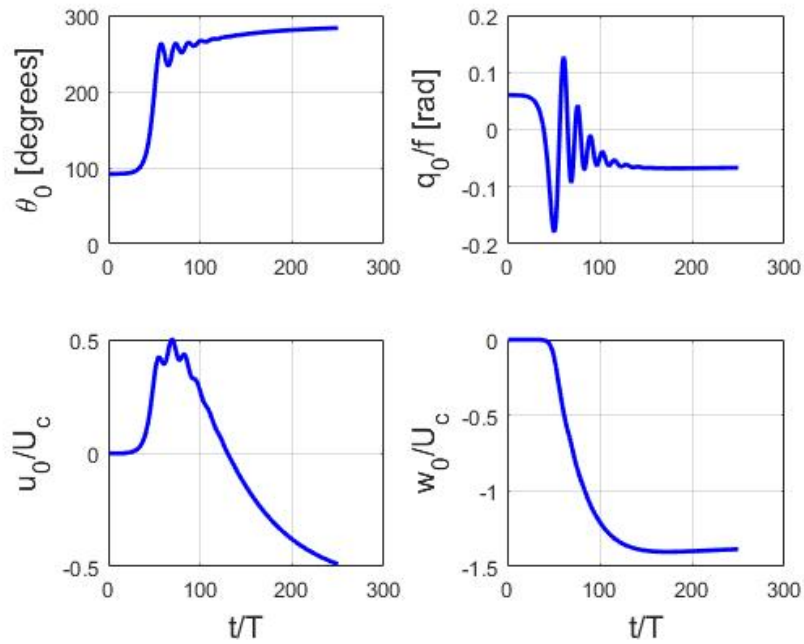
Figure 4.12: Performance of the MAV in hover for $t > T$. Subscript "0" stands for initial condition at each period.
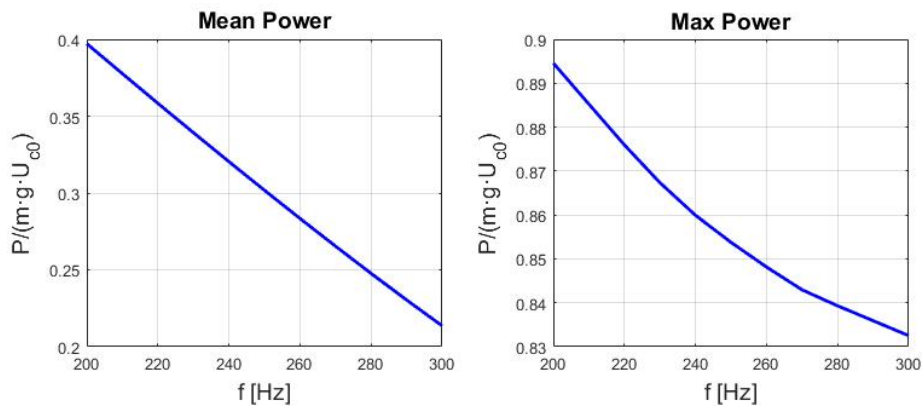
Figure 4.13: Mean consumed power and maximum peak of consumed power during a trimmed hover cycle, for different values of flapping frequency.

velocity as it will not have any penalty.

We can also observe the relation between the stroke amplitude and power, that is almost proportional to each other. It is also interesting to see how, by reducing the stroke angle the oscillations are reduced. However a lower stroke plane angle results in more oscillations of the x_G and u variables. The jump that this angle experiences at the frequency $f = 220$ may indicate that the numerical tool has changed from one solution branch to another.
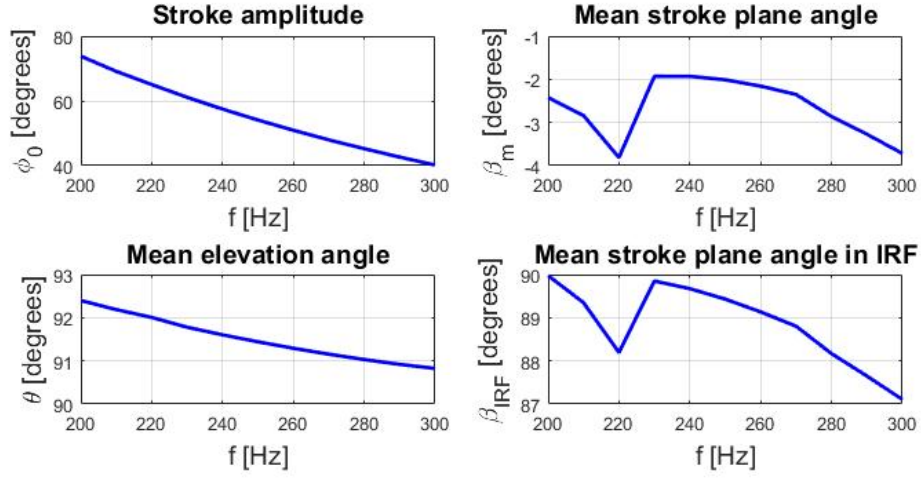
Figure 4.14: Stroke amplitude ϕ_0, mean stroke plane angle β_m, mean elevation angle θ_m and mean IRF stroke plane angle, with respect to different flapping frequencies in hover.
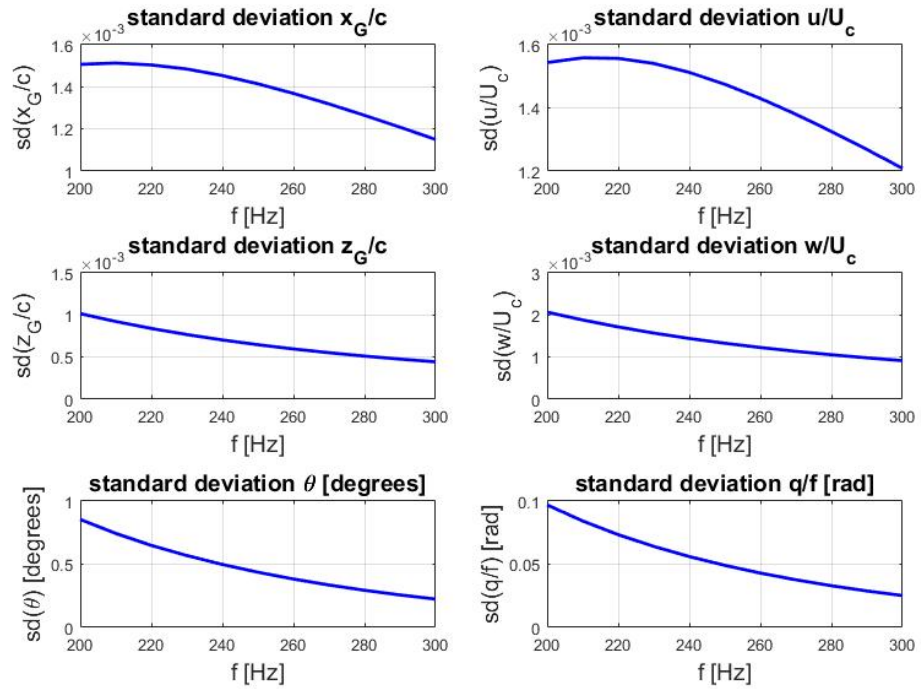
Figure 4.15: Standard deviations of some kinematics of the body, during a period of hover.

4.5 Modified aerodynamic and kinematic model

As we discussed earlier, our first model included some critical flaws that did not allow us to obtain results that were similar to the observed behaviours of insects. Thus some modifications were included in the model. In particular, the position of the attachment of the wings was changed,

and the drag of the body was modified so it only produced forces in the horizontal direction. These changes are summarized in appendix (B).

Here we present some of the results obtained with this new MAV model. Later we will compare them with the results obtained with the first one. For these new analyses, the fixed wing kinematics have been set as follows:

- Stroke plane amplitude $\beta_0 = 4°$. This is a lower value than the one used for the hover case defined before. Such a lower angle is expected to be easier to define for a future MAV.

- Geometric pitching amplitude $\alpha_0 = 70°$.

- Flapping frequency $f = 260 Hz$.

Note that the configuration of wing and wake panels is the same that was chosen above. With the new kinematic relations the new model was capable of performing hover and forward flight, and more importantly, to change smoothly from one condition to the other.
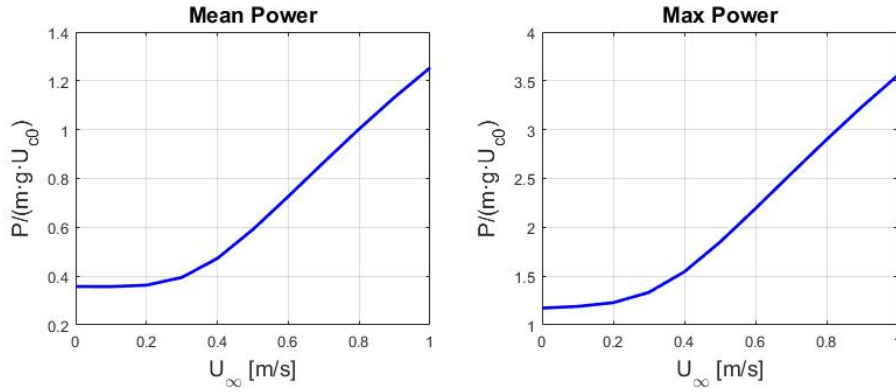
Figure 4.16: Mean consumed power and maximum peak of consumed power during a trimmed flapping cycle, for different values of absolute forward velocities calculated with the new model.

With the selected wing kinematics the vehicle can reach trimmed flight conditions for different forward flight velocities smaller than a maximum allowable one, figure (4.16). This boundary corresponds to the point at which the MAV reaches its maximum allowed stroke amplitude (consumed power), figure (4.17). It is expected that, as we vary the flapping frequency, this limit will increase, or decrease proportionally, as it was observed for the first model. Check that the point of minimum power corresponds to the hover case, when the wings only have to produce the forces that counteract the weight of the MAV, not the drag.

The value of the pitch angle defines what is the relative position of O w.r.t. G in the IRF, (4.17). This will in turn determine what are the torques that the forces of the wings attached in the former produce in the latter. So in hover, the calculated pitch angle is the one that aligns the two points vertically, figure (4.21). As the velocity increases, θ is adjusted so the total torque in G is close to 0.

The mean stroke plane angle β_m is in charge of setting the mean value of β_{IRF}, that better adjusts to each condition. This last parameter will determine what are the components of the wing forces in task of counteracting the drag and weight.
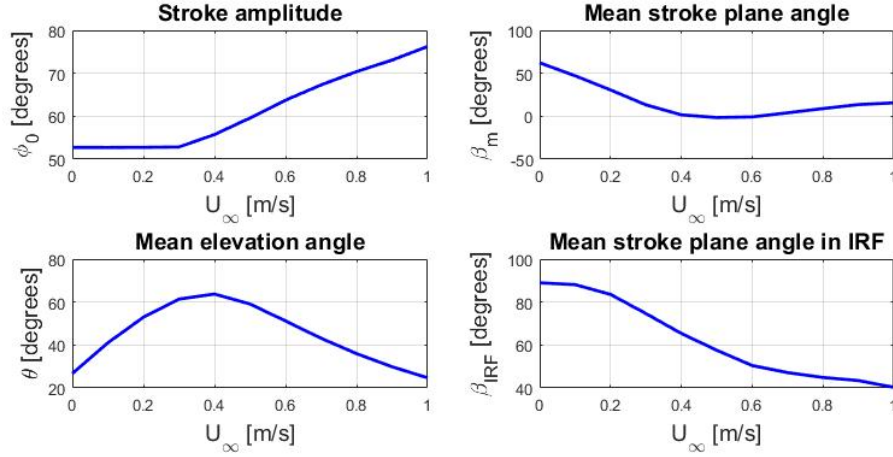
Figure 4.17: Stroke amplitude ϕ_0, mean stroke plane angle β_m, mean elevation angle θ_m and mean IRF stroke plane angle, with respect to different absolute flight velocities for the second vehicle model.
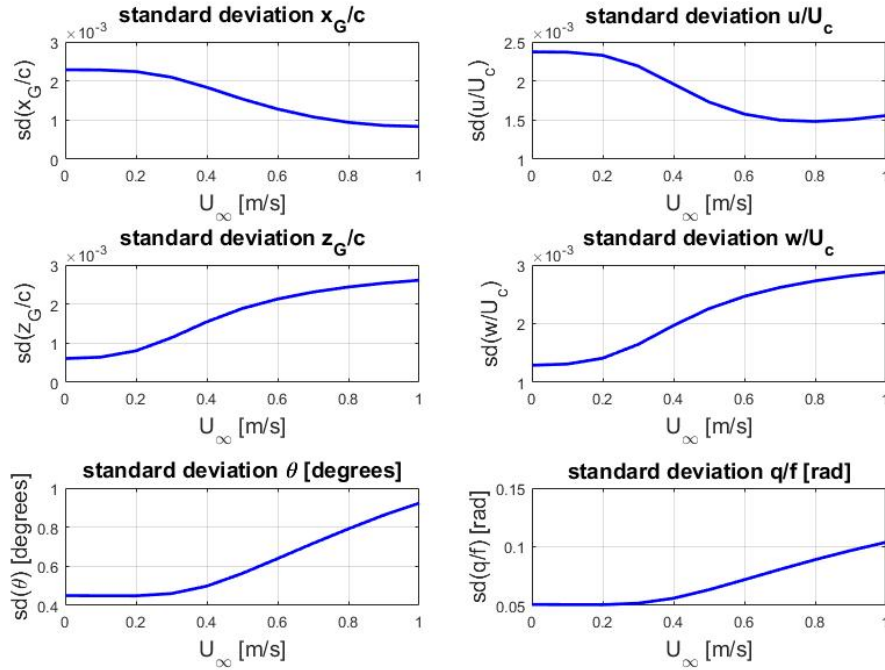
Figure 4.18: Standard deviations of some kinematics of the body, during a period of trimmed flight. The model selected is the second one, and the values depend on the absolute forward flight velocity.

The standard deviation of the position of the center of gravity x_G in figure (4.18) has been calculated with respect to an equivalent point E, that moves at a constant velocity $\vec{V}_E = [U_\infty, 0, 0]$ in the IRF.

As we increase the forward flight velocity, the wing forces present peaks of higher values, which

results in more oscillations (z_G,w). Their resultant torques at G are also increased which results in more oscillations of the pitch angle and pitch rate. However, in this new model, we have defined a drag force whose only component is parallel to the forward flight velocity u. The drag acts as a passive stabilizer of the two horizontal variables x_G and u, as its directions is always opposite to the moving direction.

4.5.1 Hover

Here we analyse the case of hover $U_\infty = 0$ that was obtained with the new MAV model.
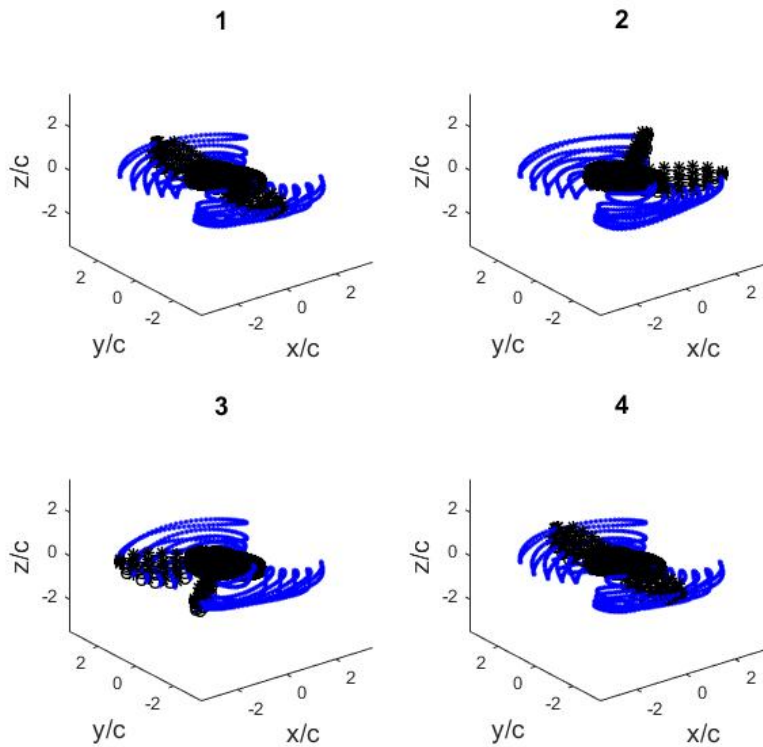
Figure 4.19: Four instants of the flapping cycle during hover using the second MAV model. In black the body and wing panels, in blue the wake. Initial position (1) $t = 0$, pronation (2), supination (3) and final position (4) $t = T$.

Find in figure (4.20) the position of G with respect to an equivalent moving point with constant IRF velocity $\vec{V}_E = [U_\infty, 0, W_\infty]$. Find indicated the instants of time for pronation (2), supination (3) with two hollow red dots, and initial, final position with a filled blue dot.

The resultant evolution of the kinematics of this second model in hover, are similar to those observed for the first one, except from the pitch angle, that, in this case is chosen so the point O is vertically aligned with G, (4.21).

As we can see from figure (4.22), during a flapping cycle, the horizontal forces and moments of the wings balance themselves. The wings are in task of providing all the lift of the vehicle.
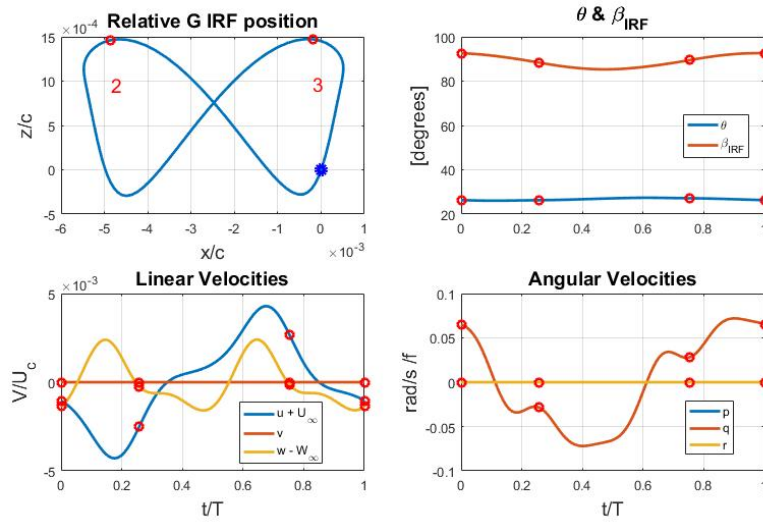
Figure 4.20: Kinematics of the MAV during 1T trimmed hover, using the second model.
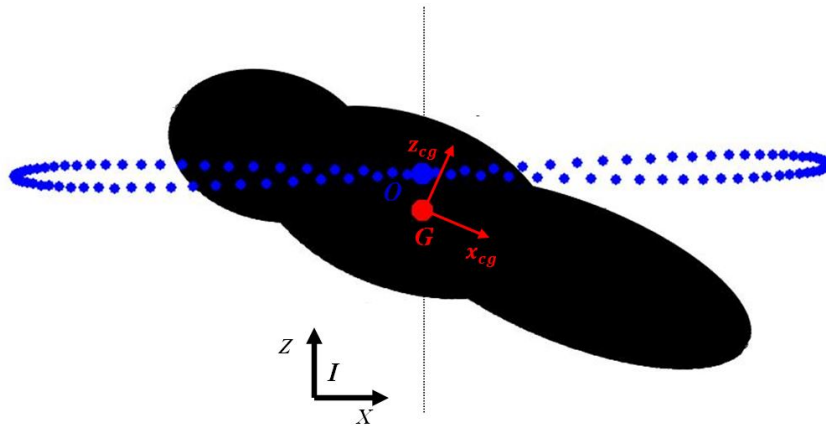
Figure 4.21: Alignment of O and G during hover of the second model. In blue the stroke of a point at the 75% of wing span, whose $x_w = 0$.

4.5.2 Forward flight

Here we analyse the case of maximum allowable forward flight velocity that was obtained with the use of the new model, $U_\infty = -1m/s$.

The top plot to the left in figure (4.24) represents the position of G with respect to an equivalent moving point E with constant IRF velocity $\vec{V}_E = [U_\infty, 0, W_\infty]$. Find indicated the instants of time for pronation (2), supination (3) with two red dots, and initial, final position with a filled blue dot.

Check that in this case, the wing forces are in task of providing both, horizontal and vertical forces, figure (4.25). Thus the mean stroke plane angle in the IRF is tilted, figure (4.24), and is no longer perpendicular to the flying direction. The attitude of the MAV is adjusted so the moments of the wings, plus the torques that result from expressing the wing forces at O in the center of
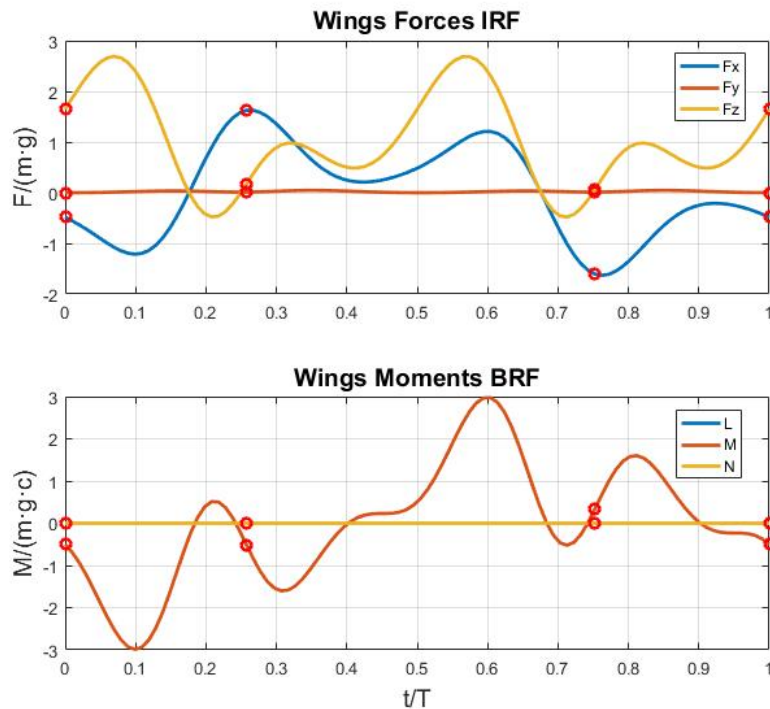
Figure 4.22: One period history of the wing forces (IRF) and moments (body axis) with the second MAV model at hover.

mass G, balance at that point.

4.5.3 Robustness analysis

It has also been studied whether our new model is also periodically stable during forward flight and hover. Find the results in figure (4.26). Please note that u_0 is the forward flight velocity, plus U_∞, at the beginning of each period.

It turns out that this model does not result in a stable behaviour, not in hover neither in forward flight, a feature that has also been observed by other studies [31]. The vertical forces of the wings produce a torque that is not counteracted by any other aerodynamic surface of the model. Although the horizontal forces are related to a torque of opposite sign, after a given set of periods, the movement becomes unstable.

4.6 Discussion between the two models

In this project, our numerical tool has worked with two models, one of them, proposed at the last stages of the project, more realistic than the original one. Despite the important flaws of the first one, it could be interesting to comment some of its characteristics and compare them with the ones of the new model.
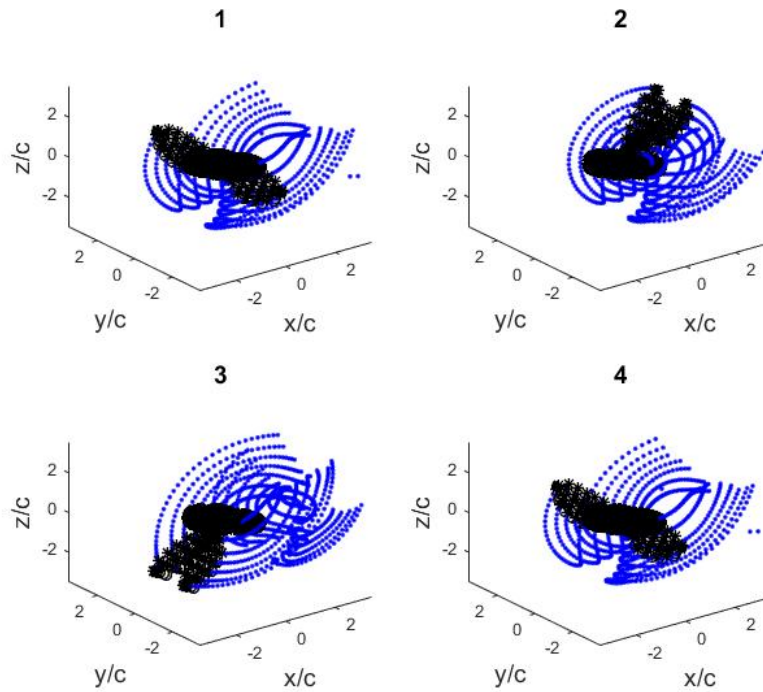
Figure 4.23: Four instants of the flapping cycle during forward flight for the second model. In black the MAV body and wing panels; in blue the wake. Initial position (1) $t = 0$, pronation (2), supination (3) and final position (4) $t = T$.
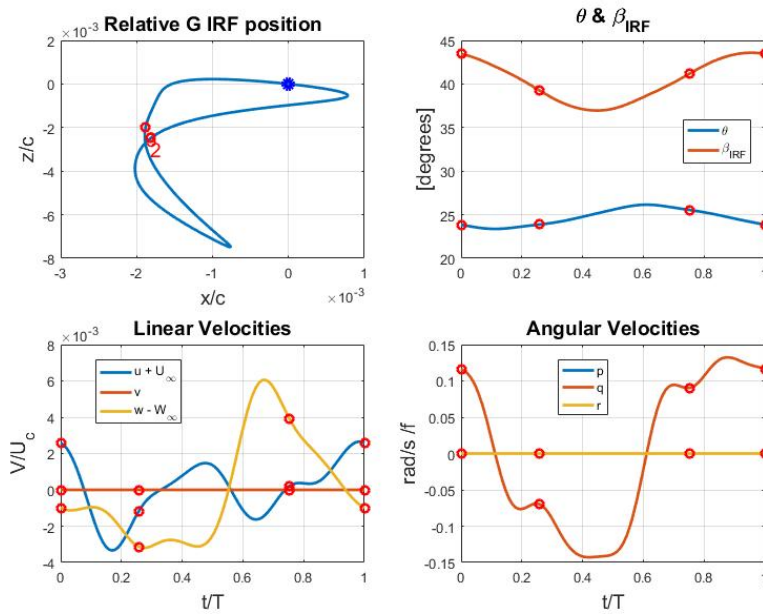
Figure 4.24: One period kinematics using the second MAV model in forward flight.
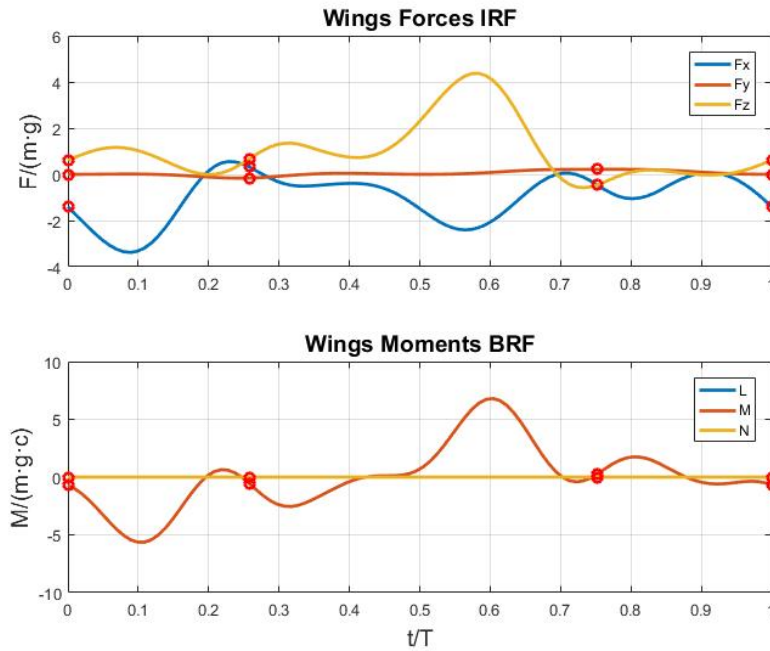
Figure 4.25: One period history of the wing forces (IRF) and moments (body axis) in forward flight using the second MAV model.
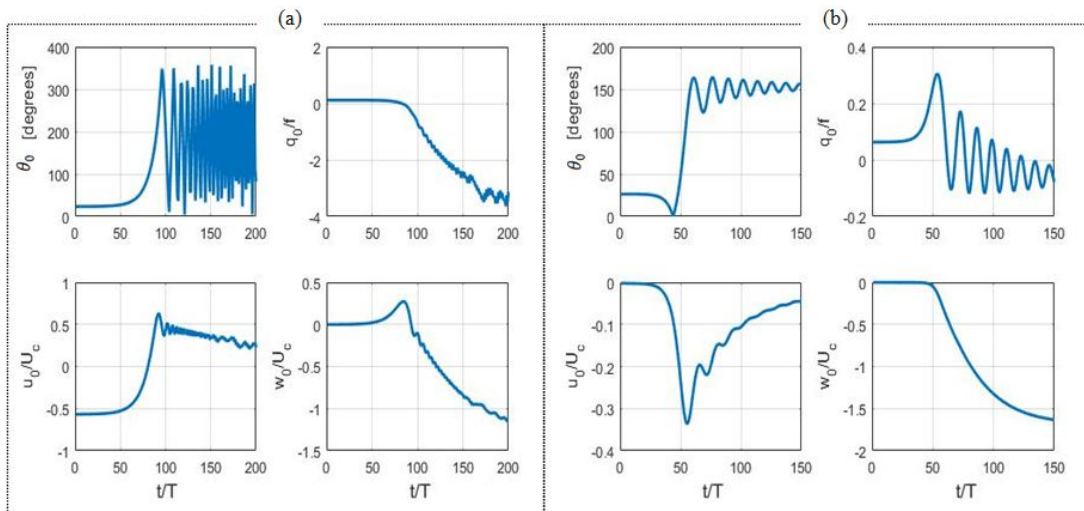
Figure 4.26: Robust analyses of the second vehicle model. (a) is the case of forward flight for $U_\infty = -1m/s$. (b) is the case of hover.

4.6.1 First model

During hover both models calculated similar behaviours, however, as soon as we added some forward flight velocity, the results of the first became clearly unrealistic, or did they?

During forward flight our first model did not approximate the characteristics of a natural flier,

however its characteristics were similar to the ones expected from a simplified air-plane model. The thrust was produced with the use of two flapping wings, since the mean stroke plane angle during this phase, was always adjusted so the forces of the wings had its component in the horizontal direction. The wings had an upper limit of available thrust, corresponding to the maximum allowable flapping amplitude.

The drag model could also be seen as a combination of the usual parasitic drag in the horizontal direction, plus the resultant lift of an aerodynamic surface attached to the body. Check that the vertical component of our body drag greatly depended on the pitch angle of the MAV.
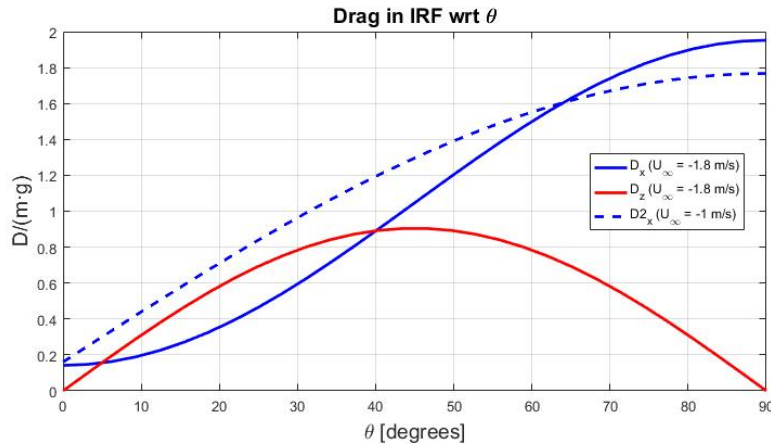
Figure 4.27: Evolution of the body drag w.r.t. θ using both models, at approximately the maximum flight velocities of the two cases. D2 stands for the second model.

Find in figure (4.27) in solid lines the components of the body drag of the first model, D_x and D_z in the X and Z directions of the IRF. Find in a dashed line the solely component of the drag of the second model $D2_x$ in the X direction of the IRF.

Using the first model, at a pitch angle equal to 0, no body drag would be directed upwards. As we increase the angle, the vertical component also increases, until it reaches a maximum. It could be argued that the evolution of our vertical body drag with respect to θ, is similar to a simple aerodynamic model of an air-plane, that relates the lift coefficient of a wing with its angle of attack.

Check that the performance of our model, in terms of forward flight velocity, is limited by a pair of boundaries similar to the ones found in the performance of some air-planes: an upper value related with the maximum available thrust, and a minimum value that depends on the maximum allowable pitch angle.

4.6.2   Second model

Despite the second model does not take into account some features as the drag of the wings or some of the unsteady mechanisms that the MAV uses to enhance its aerodynamic forces, it allowed us to obtain more realistic results than the first one.

So, while a typical air-plane is not able to reduce its velocity from a certain value (first model), our MAV can perfectly sustain hover and, at a certain instant of time, it can adapt its stroke parameters to change smoothly to a forward flight condition. Thus the vehicle can rapidly manoeuvre to go from one condition to another.

Check that, despite the maximum allowed forward flight velocities of the first model are higher than the ones of the second, the differences are not that big. If we also take into account the manoeuvring possibilities of the latter with respect to the highly restricted performance of the former, it can be concluded that a flapping wing MAV design represents a better choice than a fixed wing one for these flight conditions.

Chapter 5

Conclusions

During this project we have developed a numerical tool that integrates a pre-existing unsteady panel method and a dynamic model to obtain trimmed flight conditions for different MAV models. In fact, the tool was able to trim two different models, and it allowed us to perform some parameter analyses.

By making use of the resultant tool, we have determined how the performance of the vehicle depends on some imposed parameters, and points of minimum power and oscillations. The numerical scheme has also allowed us to detect what were the performance limits of some configurations, and the need to change some aspects of the wing kinematics to reach other flight conditions.

Overall the tool has proven to be a cost-effective asset. The computation time of our *nominal case* (that iterated $\sim 10^3$ variables) was of approximately 40 minutes, for a laptop with an iCore7 processor working at 2.9 GHz. It is expected that, with a better tuning of the tool, and a simplification of the code, the time can be reduced.

5.1   Future works

Apart from improving the presented models, future works shall also focus on the possibility of defining a better MAV geometry, which could get rid of the stroke amplitude limitation. This was found to be a major issue, as, the GMRES method could not be told to ignore the associated residual of the stroke amplitude, and to focus on other variables when the limit was reached.

We have also been working with Reynolds numbers with very low values for a potential flow theory point of view. Viscous effects should also be taken into account as in such a regime they are expected to play major roles.

Moreover, we have also studied how a drag model, roughly similar to a fixed wing model, was able to obtain higher forward flight velocities than the more accurate one. It could be interesting to study the possibility to design a shape shifting flapping MAV, that, when it reached a certain forward flight velocity, would unfold a wing or aerodynamic surface that could produce the required lift of the MAV.

Another interesting idea is to combine our models with an aero-elastic code that would also take into account deformations of our wings. In that case, the numerical tool will be fed with new periodic equations to be fulfilled. We already know that some elastic features enhance the value of the forces [30], and we are starting to see how important flexibility may be for flight stability [7].

The final goal would be to combine the perfected models, our numerical tool and some control laws to build a numerical scheme that could ultimately allow us to create a complete and autonomous flapping MAV.

As Mark Twain put it:

> *The secret of getting ahead is getting started.*

Appendix A

Initial guess

In order to start the GMRES method, we need to feed it with an initial guess of the target vector $\vec{q}_0$. Although this initial vector could be set manually, it is more convenient to be able to calculate it in a way such that it is as similar as possible to the expected final one, so the time it takes the method to converge is as small as possible. In this project two ways to determine a first guess are presented, and the use of one or another depends on whether the analysis to be performed is a completely new one, or if it is very similar to a one already performed.

A.1   Static procedure

When a new analysis is going to be performed we can only count on intuition to determine what the final attitude and velocity of the MAV are going to be. By a new problem we mean one whose set of fixed parameters is not similar to any of the previous analyses. Remember that the fixed parameters were:

$$f, U_\infty, W_\infty, \alpha_0, \beta_0, \text{plus the geometric and mass characteristics}$$

Our state vector not only includes the initial attitude and velocities of the MAV, but also its developed wake, and wing circulation of previous instants of time. Let us split the definition of the initial state vector in 2 steps:

- Firstly we can set the initial attitude (quaternion) and velocities of the MAV: $Q_0, u_0, w_0, \dot{\theta}_0$, and an initial guess of the mean stroke plane β_m and stroke amplitude ϕ_0. It is highly recommended to directly define the velocities as: $u_0 = \pm U_\infty$ and $w_0 = \pm W_\infty$.

- Then we can impose a movement of constant velocities u_0, w_0 and constant attitude Q_0, during which the MAV flaps its wings as it has been defined. That movement is imposed during a time $t = n \cdot T$ with $n > 1$ after which not only the wake is completely developed $i_{wake} = i_{wake_{max}}$, but it also had time to become as periodic as possible. In other words the vehicle is forced to move in a given direction, without taking into account its aerodynamic forces.

A.2　Continuation procedure

On the other hand, as soon as we have a solution for a given set of flight conditions, we can use another approach to calculate the initial guess of following analysis. When what we want is to check what is the effect of slightly varying one of the fixed parameters listed above, or, with the same conditions, to change the number of wing or wake panels, instead of using the above described *Static procedure*, we can use the already calculated solution as the initial guess.

A given solution of our problem is associated with a resultant one period time history of the movement of the vehicle. By imposing this movement to our new conditions, we can create a new state vector.

By using this *Continuation procedure* on analyses pretty similar to already calculated ones, we obtained initial state vectors more similar to the final solution than those obtained by using the *Static procedure*. In fact, when using the former, the computation time was reduced by a half in average, reaching a quarter for some cases.

Appendix B

Modification of the MAV model

After unveiling the drawbacks of the first body drag model, another option had to be proposed. In order to do that, apart from the parasitic drag, some other features of our MAV model had to be changed.

B.1   New body drag model

The defined parasitic drag model proved to be an unrealistic one, as the forces not only acted in the direction of the free stream velocity, but also helped to keep the MAV aloft. So a new model was defined, that calculated a drag force whose only component will point opposite to the forward flight velocity u. This new drag will have a magnitude defined as:

$$D = \frac{1}{2}\rho u^2 L_{body} D_{body} C_D \tag{B.1}$$

The product $L_{body} \cdot D_{body}$ gives us a conservative value of the reference surface of the body of the vehicle, while C_D is the drag coefficient, that depends on the attitude of the MAV. The formula to calculate the coefficient was determined to be:

$$C_D = C_{D_m} + C_{D_0} \cdot |\sin(\theta)| \tag{B.2}$$

Where C_{D_m} is equal to our initial 0.8, and C_{D_0} is equal to 8. This value was chosen so the maximum drag (at a velocity $U_\infty = -1m/s$) was similar to the weight, so the wing forces must be directed in both directions simultaneously. Remember that at $Re \sim 10^2$ the values of the drag coefficient are of the order of unity, and that real life fruit flies do not usually fly at velocities higher than $0.85m/s$, [32].

B.2   New geometry

We have been working with two wings attached to a point O, whose position with respect to G is given by the vector:

$$\vec{x}_{O/G} = \begin{bmatrix} x_{O/G} \\ y_{O/G} \\ z_{O/G} \end{bmatrix} \tag{B.3}$$

The elements of our first vector $\vec{x}_{O/G}$ were all equal to 0 except from $x_{O/G}$. The reason that, with this overshoot, we did not see any instability, is that the contribution of the vertical wing forces to the angular equilibrium was found to be negligible, or perfectly balanced with the much higher horizontal forces. However, with this new body drag model, all the vertical forces are going to be provided by the wings, so, their associated torque at the center of mass G, could lead to an unstable behaviour.

The wings are not only in task of providing lift, but also thrust, which will try to point in the direction of the forward flight velocity. Check that if we add a value $z_{O/G}$ bigger than 0, we can also obtain a torque in G for any pitch angle. This torque will have a value of opposite sign to the one produced by the wing forces.

Thus the elements of vector $(B.3)$ have been redefined as:

$$x_{O/G} = -0.1 D_{body} \tag{B.4}$$

$$y_{O/G} = 0 \tag{B.5}$$

$$z_{O/G} = 0.2 D_{body} \tag{B.6}$$

Appendix C

Project Budget

Find in this appendix an estimation of the budget of the project.

- **MATLAB license**. All the simulations presented in this project have been performed using the program MATLAB Ⓡ. An individual academic license currently costs 500 €.

- **Computational cost**. Due to the high number of simulations, the calculations have been made with the use of a High Performing Computer Cluster. Currently Spanish CESGA centre offers their clusters at an average price of 0.10 €per CPU per hour. The total hours of computation in this project are estimated to be close to 500h, at 2CPU. The total computational cost is of 100 €.

- **Personal computer**. The data processing, and some preliminary analyses were performed with a personal laptop *Lenovo* with an Intel(R) Core(TM) $i7 - 3520M$ processor, currently priced at 566 €.

- **Worker salary**. The estimated income per hour of a junior engineer in Spain is estimated to be 11 €. The time invested in the project is of around 700h resulting in a total of 7700 €.

The total budget of the project is estimated to be close to: 8866 €.

Bibliography

[1] AESA. Drones / marco regulatorio. `http://www.seguridadaerea.gob.es/lang_castellano/cias_empresas/trabajos/rpas/marco/default.aspx`, 2014. (Accessed on 08/06/2017).

[2] David E. Alexander. *Nature's Flyers*. The Johns Hopkins University Press, 2002.

[3] SA Ansari, R Żbikowski, and Kevin Knowles. Aerodynamic modelling of insect-like flapping flight for micro air vehicles. *Progress in Aerospace Sciences*, 2006.

[4] Gonzalo Arranz. Development of an unsteady potential model for a flapping wing mav., 2015. End of degree project, Universidad Carlos III de Madrid.

[5] Camli Badrya and James D. Baeder. Insect kinematics in trimmed flight at low reynolds numbers using cfd. In *53rd AIAA Aerospace Sciences Meeting*, 2015.

[6] James Bluman and Chang-Kwon Kang. Wing-wake interaction destabilizes hover equilibrium of a flapping insect-scale wing. *Bioinspiration and Biomimetics*, 2017.

[7] James Edward Bluman. *The effects of wing flexibility on the flight performance and stability of flapping wing micro air vehicles*. PhD thesis, The University of Alabama in Huntsville, 2017.

[8] Richard J. Bomphrey, Toshiyuki Nakata, Nathan Phillips, and Simon M. Walker. Smart wing rotation and trailing-edge vortices enable high frequency mosquito flight. *Nature*, 2017.

[9] Bo Cheng and Xinyan Deng. Translational and rotational damping of flapping flight and its dynamics and stability at hovering. *IEEE Transactions on Robotics*, 2011.

[10] G.C.H.E. de Croon, M. Percin, B.D.W. Remes, R. Ruijsink, and C. De Wagter. *The DelFly design, aerodynamics, and artificial inteligence of a flapping wing robot*. Springer, 2016.

[11] Michael H Dickinson and Karl G Gotz. Unsteady aerodynamic performance of model wings at low reynolds numbers. *Journal of Experimental Biology*, 1993.

[12] EASA. Civil drones (unmanned aircraft). `https://www.easa.europa.eu/easa-and-you/civil-drones-rpas`, 2017. (Accessed on 08/06/2017).

[13] Dario Floreano and Robert J Wood. Science, technology and the future of small autonomous drones. *Nature*, 2015.

[14] Dario Floreano, Jean-Christophe Zufferey, Mandyam V. Srinivasan, and Charlie Ellington. *Flying insects and robots.* Springer, 2009.

[15] William Ford. *Numerical linear algebra with applications.* Elsevier Inc, 2015.

[16] Steven N Fry, Rosalyn Sayaman, and Michael H Dickinson. The aerodynamics of hovering flight in drosophila. *Journal of Experimental Biology*, 2005.

[17] R. J. Full and M. A. R. Koehl. Drag and lift on running insects. *Journal of Experimental Biology*, 1993.

[18] Na Gao, Hikaru Aono, and Hao Liu. Perturbation analysis of 6dof flight dynamics and passive dynamic stability of hovering fruit fly drosophila melanogaster. *Journal of theoretical biology*, 2011.

[19] David Grimaldt and Michael S.Engel. *Evolution of the insects.* Cambridge University Press, 2005.

[20] Drone industry insight Co. Insights. `https://www.droneii.com/`, 2015. (Accessed on 15/06/2017).

[21] Joseph Katz and Allen Plotkin. *Low-speed aerodynamics.* Cambridge University Press, 2001.

[22] Lian Pin Koh and Serge A Wich. Dawn of drone ecology: low-cost autonomous aerial vehicles for conservation.

[23] Hao Liu, Sridhar Ravi, Dmitry Kolomenskiy, and Hiroto Tanaka. Biomechanics and biomimetics in insect-inspired flight systems. *Phil. Trans. R. Soc. B*, 2016.

[24] Yanpeng Liu and Mao Sun. Wing kinematics measurement and aerodynamics of hovering droneflies. *Journal of Experimental Biology*, 2008.

[25] Blanca Martínez. Dynamic models for flapping-wing micro-air vehicles., 2015. End of degree project, Universidad Carlos III de Madrid.

[26] Umberto Pesavento and Z. Jane Wang. Flapping wing flight can save aerodynamic power compared to steady flight. *Phys. Rev. Lett.*, 2009.

[27] Hoang Vu Phan, Taesam Kang, and Hoon Cheof Park. Design and stable flight of a 21 g insect like tailless flapping wing micro air vehicle with angular rates feedback control,. *Bioinspiration & Biomimetics*, 2017.

[28] Leif Ristroph, Gunnar Ristroph, Svetlana Morozova, Attila J Bergou, Song Chang, John Guckenheimer, Z Jane Wang, and Itai Cohen. Active and passive stabilization of body pitch in insect flight. *Journal of The Royal Society Interface*, 2013.

[29] Alana Sherman and Michael H Dickinson. A comparison of visual and haltere-mediated equilibrium reflexes in the fruit fly drosophila melanogaster. *Journal of Experimental Biology*, 2003.

[30] Wei Shyy, Hikaru Aono, Chang-Kwon Kang, and Hao Liu. *An introduction to flapping wing aerodynamics.* Cambridge University Press, 2013.

[31] Mao Sun. Insect flight dynamics: stability and control. *Reviews of Modern Physics*, 2014.

[32] Mao Sun and Jiang Hao Wu. Aerodynamic force generation and power requirements in forward flight in a fruit fly with modeled wing motion. *Journal of Experimental Biology*, 2003.

[33] Graham K Taylor. Mechanics and aerodynamics of insect flight control. *Biological Reviews*, 2001.

[34] Zhi Ern Teoh, Sawyer B Fuller, Pakpong Chirarattananon, NO Prez-Arancibia, Jack D Greenberg, and Robert J Wood. A hovering flapping-wing microrobot with altitude control and passive upright stability. In *Intelligent Robots and Systems (IROS), 2012 IEEE/RSJ International Conference on*. IEEE, 2012.

[35] Ashish Tewari. *Atmospheric and space flight dynamics*. Birkhäuser, 2007.

[36] V. B. WIGGLESWORTH. *THE PRINCIPLES OF INSECT PHYSIOLOGY*. Chapman and Hall Ltd, 1972.

[37] Donald F. Young, Bruce R. Munson, Theodore H. Okiishi, and Wade W. Huebsch. *A brief introduction to fluid mechanics*. John Wiley and Sons, Inc, 1988.